Physics of Fluids

RESEARCH ARTICLE | JUNE 25 2025

Improving dynamic mode decomposition of tandem cylinder flow with nonlinear dictionaries

A. D. G. Hales; M. J. Colbrook; C. Jiang

Physics of Fluids 37, 067154 (2025)
https://doi.org/10.1063/5.0271497

Improving dynamic mode decomposition of tandem cylinder flow with nonlinear dictionaries

Cite as: Phys. Fluids 37, 067154 (2025); doi: 10.1063/5.0271497
Submitted: 18 March 2025 · Accepted: 17 April 2025 ·
Published Online: 25 June 2025

A. D. G. Hales,[1,a)] M. J. Colbrook,[2] and C. Jiang[3]

AFFILIATIONS

[1]Department of Aerospace & Ocean Engineering, Virginia Tech, Blacksburg, Virginia 24060, USA
[2]Department of Applied Mathematics and Theoretical Physics, University of Cambridge, Cambridge CB3 0WA, United Kingdom
[3]Department of Mechanical and Manufacturing Engineering, UNSW Sydney, Sydney, NSW 2052, Australia

[a)]Author to whom correspondence should be addressed: adgh3@vt.edu

ABSTRACT

This paper examines algorithmic nonlinear dictionary enhancements for dynamic mode decomposition (DMD) based analysis of an industrially relevant flow problem. Several nonlinear variants of DMD are used to analyze flow interacting with two tandem cylinders in a bi-stable configuration. This study investigates the coexistence of two vortex shedding regimes, distinguished by their characteristic frequencies. Using DMD, we extract coherent structures associated with each regime and consider their relation to surface pressure and far-field noise at these frequencies. Simultaneous experimental measurements of velocity fields, unsteady surface pressure, and far-field acoustic pressure are performed using high-speed particle image velocimetry, a remote microphone technique, and a far-field microphone. Two DMD algorithms are applied to investigate the flow. First, we apply kernelized extended DMD to demonstrate how a nonlinear dictionary can improve modal reliability compared with the usual linear alternative. The extracted modes are validated by analyzing their modal residuals, which are further used to explore phenomena at other frequencies and harmonics while examining the impact of dictionary depth and characteristics. Second, we study the flow physics of each shedding frequency via the Rigged DMD algorithm, which provides detailed spectral insights for dynamical systems with continuous spectra. A new kernelized Rigged DMD is introduced, showing improved accuracy in resolving generalized eigenfunctions and spectral measures compared to linear dictionaries.

I. INTRODUCTION

Dynamic mode decomposition (DMD) is a popular tool to extract dominant flow characteristics and dynamics.[1–3] It was developed as a data-driven method to approximate the Koopman operator of trajectory data.[4,5] The Koopman operator linearizes a nonlinear dynamical system, allowing representation through successive experimental snapshots.[6] DMD has proven to be a powerful and versatile tool in fluid dynamics research. The development of improved algorithms provides insight into physical applications in fluids[7] and, in turn, can also be influenced by applications. Such applications include, but are not limited to, cylinder wake studies,[8–11] cavity flows,[3,12–14] and the tandem cylinder flow interaction problem,[15–17] which will be the focus of our study.

Flow interaction with tandem cylinders is a classical problem in fluid mechanics, associated with various phenomena that include vortex shedding, wake dynamics, and acoustic radiation. Extensive research has been conducted on this topic,[18–22] aiming to understand the diverse flow physics exhibited. In particular, several flow regimes arise depending on the spacing between the two cylinders. Understanding the flow phenomena in these interactions is relevant for civil and ocean engineering applications. In addition, analyzing the noise generated is crucial for aeroacoustics, especially due to the presence of cylinders in landing gear and airframes.[23,24] The noise generated when flow interacts with tandem cylinders has been the focus of experimental and numerical studies,[25–28] in which porous coatings are used as an effective strategy for noise-reduction.

When two cylinders are positioned with a critical spacing, the flow over tandem cylinders can exhibit bi-stability,[29,30] wherein the flow alternates between two distinct quasi-stable regimes. This phenomenon has implications for noise generation, structural vibrations, and heat transfer, which is of considerable interest to engineers. However, the bi-stable nature and the interactions between wake dynamics and far-field noise remain poorly understood, particularly in real-world configurations that involve turbulent flows. These complex dynamics are particularly suited to DMD since the transition between regimes and the respective harmonics can be captured by distinct modes and studied for their properties. However, relating modes associated with vorticity to other observables, such as surface or far-field pressure, is a more challenging task.

Recent experimental studies on flow interactions with tandem cylinders in bi-stable configurations include Refs. 31–37 with Refs. 31 and 32 focusing on experiments involving cylinders of different diameters. Variations of this problem that have been studied include square cylinders[38–40] and configurations using multiple cylinders placed in a range of arrangements.[41–44] High-fidelity numerical simulations, as performed in Refs. 45–53, have also become a popular approach to understanding the complex flow physics that underlies the observed phenomena. Numerical simulations provide high-resolution data that are often challenging to capture experimentally, allowing easy adjustments to initial and boundary conditions for parameter studies. Simulations, while computationally expensive, rely on assumptions that may not reflect real-world conditions. Experiments validate them.

Previous near-field velocity measurements have been limited by intrusive or non-time-resolved techniques.[54–58] Thus, experimental methodology involving both velocity and pressure measurements is of significant interest to the field for understanding correlations between coherent vortical structures and generated noise. One method to investigate modal correlation with pressure signals, based on canonical correlation analysis, is presented in Ref. 59.

This study involves an advanced experimental setup capable of time-resolved, simultaneous measurements of near-field velocity, unsteady surface pressure, and far-field acoustic pressure. These experimental data are suitable for applying innovative DMD techniques to bring new light to the area. We examine a tandem cylinder configuration in an anechoic wind tunnel with a high-speed particle image velocimetry (PIV) system and instruments for unsteady surface pressure and far-field noise measurements. The cylinders are spaced at 3.7D (D is the diameter of both cylinders), creating a bi-stable flow state where two vortex shedding regimes alternate at distinct frequencies.[29,30] Flow structures associated with surface pressure fluctuations and far-field noise are identified using cross correlation analysis and are compared to equivalent DMD modes.

To improve the accuracy of our comparable DMD modes, we utilize several variants of DMD and present a novel algorithm that leverages the advantages of each approach. Since its inception, numerous DMD variants have emerged, thoroughly reviewed in Refs. 7 and 60. This paper focuses on three key variants: kernelized extended DMD (kEDMD),[61] Residual DMD (ResDMD),[62–64] and Rigged DMD.[12] We briefly introduce each in turn.

Extended DMD (EDMD)[65] is a generalization of DMD that enables the use of nonlinear basis functions to approximate the eigenfunctions of the Koopman operator. kEDMD[61] builds on this by associating a kernel function with the EDMD dictionary, helping to mitigate the curse of dimensionality—particularly beneficial when handling high-dimensional state spaces, as often encountered in fluid experiments. Moreover, capturing complex nonlinear flow features demands a nonlinear dictionary.

ResDMD was developed as an alternative algorithm with built-in error control.[62,66] The residual is an error measure for each eigenpair, indicating whether a mode faithfully represents the true dynamics. (It can also be used to compute general spectral properties of Koopman operators.) Given that finite-dimensional approximations of the infinite-dimensional Koopman operator can produce spurious modes, residuals provide critical error control for eigenvalues grounded in convergence theorems. We implement the residual within both the kEDMD and RiggedDMD frameworks.

Rigged DMD[12] is designed to construct smoothed generalized eigenfunctions of the Koopman operator and approximate the system's spectral measure. The spectral measure effectively diagonalizes the Koopman operator when the underlying system is measure-preserving, providing insights into its power spectrum.[62] A key advantage of Rigged DMD is its efficient and flexible calculation of generalized eigenfunctions (modes) at any spectrum point, equivalently, at any frequency relevant to the data's power spectrum, with adjustable accuracy via a tailored wavepacket approach. Demonstrated applications include high-Reynolds lid-driven flow in a square cavity and the Lorentz system.[12] Further investigation is needed to evaluate the algorithm's dependence on the initial dictionary and directly compare kEDMD and Rigged DMD in experimental contexts.

This paper demonstrates a clear improvement in modal analysis by implementing nonlinear dictionaries within RiggedDMD. The modes are verified to be physically meaningful when compared with coherence modes between vorticity and far-field noise data. These improvements are supported by calculating modal residuals, demonstrating the benefits of implementing a means of error control within machine learning. Finally, we introduce a fundamental new algorithm for investigating the properties of fluids by combining the advantages of the three aforementioned DMD variants. The new algorithm, kernelized Rigged DMD (kRigged DMD), implements nonlinear dictionaries and estimates residuals of eigenfunction within a Rigged DMD framework. This approach enhances modal accuracy for high-rank approximations over kEDMD. The primary benefits of this algorithm are:

- Efficient generation of wavepacket approximations to eigenfunctions with pre-selected levels of smoothing. This can be done even in the presence of continuous spectra.
- Permits the pre-selection of *any* frequency for an eigenfunction. These can be chosen by computing the spectral measure *or* by testing the residuals of a large sample of test eigenvalues.
- Produces physically meaningful modes whose residuals are lower on average than kEDMD for high-rank approximations.

This paper is structured as follows. We begin in Sec. II with an overview of the experimental methodology for obtaining two-dimensional, time-resolved velocity data synchronized with surface and far-field pressure measurements. Next, in Sec. III, we briefly review kEDMD, discussing key concepts adapted for our investigation. This section includes a preliminary low-rank application of kEDMD to velocity data, identifying key modes and exploring the impact of nonlinear dictionaries within the kEDMD framework. In Sec. IV, we conduct a detailed comparison of kernels with an expanded dictionary size N, enabling the analysis of additional nonspurious modes. This is followed by the development and implementation of kRigged DMD in Sec. V. We discuss this new algorithm in depth, demonstrating its ability to produce meaningful modes, which are further validated through cross correlation analysis of experimental velocity and pressure data. Finally, we compare different kernels and dictionary sizes within the kRigged DMD framework in Sec. VI, highlighting its advantages over kEDMD for identifying a broader range of modes with larger dictionaries.

II. EXPERIMENTAL METHODOLOGY

To validate these methods, we took measurements in the UNSW Anechoic Wind Tunnel (UAT), an open-jet wind tunnel with a 0.455×0.455 m test section housed within a $3 \times 4.7 \times 2.15\,\text{m}^3$ anechoic chamber with a cutoff frequency of 300 Hz. Further details on the UAT are available in Ref. 67. Figure 1 shows the wind tunnel schematics. We tested a tandem cylinder configuration with a cylinder diameter of $D = 20$ mm and a gap of $3.7D$ in the open-jet test section of the UAT. The freestream velocity was set at $U_\infty = 15$ m/s, resulting in a Reynolds number of $Re_D = 20\,000$ based on the cylinder diameter. Figure 2 illustrates the experimental setup.

We placed a VEO 640L camera on the side of the test section to take high-speed planar PIV measurements on the streamwise plane (x–y plane) at the cylinder midspan. A LaVision aerosol generator produces seeding particles with an average diameter of $\approx 1\,\mu$m. A Litron LD25-527 PIV laser system supplies illumination for PIV measurements with a maximum output energy of 25 mJ per pulse at 1 kHz. We control the data acquisition and synchronization between the laser and camera using a LaVision Programable Timing Unit (PTU X). Figure 2 shows these experimental schematics. We recorded PIV images at a sampling rate of 1 kHz with a resolution of 2560×1192 pixels and processed these results using a final interrogation window size of 32×32 with a 50% overlap.

The instantaneous vorticity flips between two stable regimes: the co-shedding and reattachment regimes. We show a representative snapshot for the co-shedding regime in Fig. 3(a). It is characterized by the shedding of vortices by both cylinders. The vortices shed by the upstream cylinder convect downstream and interact with those shed by the downstream cylinder. This leads to oscillations in the wake that contribute to far-field noise due to vortex interactions. Figure 3(b) represents the reattachment regime. This regime is characterized by two shear layers emanating from the upper and lower sides of the upstream cylinder and remaining attached to the downstream cylinder. In this regime, vortex shedding by the upstream cylinder is mostly suppressed, while vortex shedding from the downstream cylinder is also weaker and restricted to regions behind the downstream cylinder. This suppression of shedding leads to lower far-field noise levels. When the flow transitions between these two states, observed far-field noise and pressure fluctuations are expected to change drastically. The shear layers either stabilize or break down, while the onset of vortex shedding either begins or significantly weakens. We couple our DMD-based investigation into the flow vorticity with synchronized pressure and far-field noise measurements to understand how the flow physics observed during these transitions relates to changes in surface pressure or far-field noise.

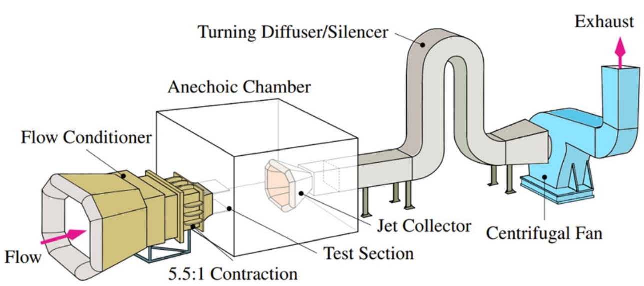

FIG. 1. Schematic of the UNSW anechoic wind tunnel (UAT).

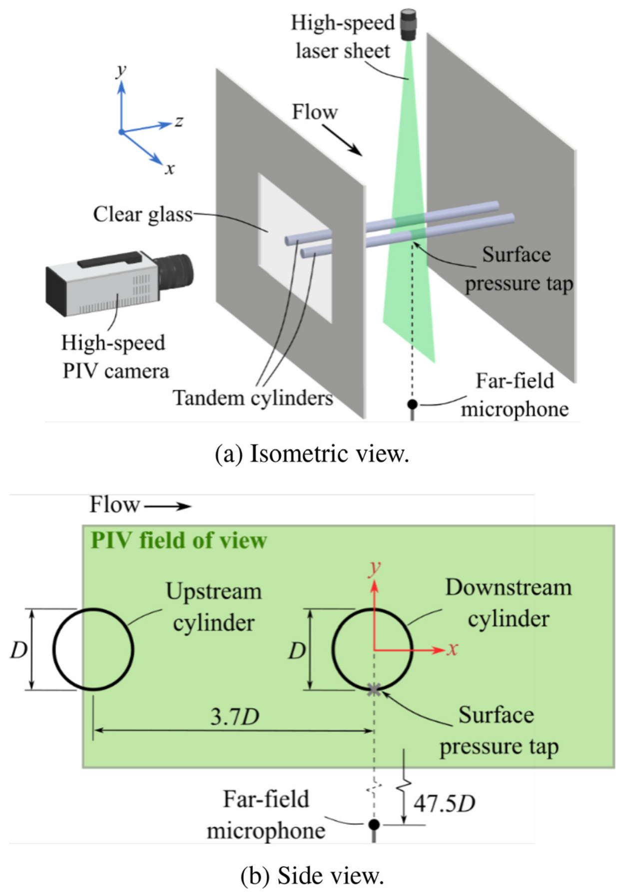

FIG. 2. Schematics of the experimental setup.

We acquired unsteady surface pressure data using a remote microphone technique,[68,69] equipped with a GRAS type 40 PH 1/4 in. microphone. We recorded all microphone signals at a sampling rate of 40 kHz using a National Instruments PXI platform, while PIV measurements were made. The synchronization between PIV data and pressure signals was achieved using the camera trigger signal measured from the PTU X. We acquired far-field acoustic data using a GRAS type 40 PH 1/4 in. microphone placed 0.95 m ($47.5D$) underneath the midspan of the downstream cylinder. The surface pressure tap (0.9 mm diameter) is located in the midspan of the downstream cylinder, facing the far-field microphone (azimuth angle of 270°).

The PSD for the far-field noise and the surface pressure are plotted in Fig. 4. The two shedding frequencies at approximately 100 and 130 Hz have significant peaks for both PSDs. We notice significant

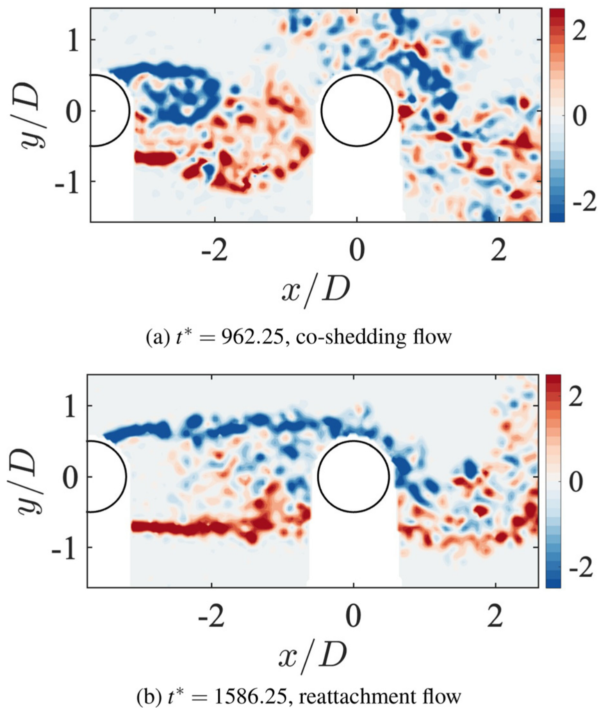

(a) $t^* = 962.25$, co-shedding flow

(b) $t^* = 1586.25$, reattachment flow

FIG. 3. Instantaneous vorticity snapshots of the co-shedding and reattachment regimes, normalized by $\omega D/U_0$, at specific times $t^* = tU_0/D$.

peaks for either or both PSDs when looking at the higher frequency harmonic (integer multiples of these two shedding frequencies).

Figure 5 shows the evolutionary power spectral density (EPSD) for the vorticity signal averaged along the line $x/D = 1.0$. We take this EPSD in the gap to observe both regimes. The first shedding frequency is related to the vortex shedding present at the reattachment regime, while the second peak relates to the co-shedding regime. Between $t^* = 700$ and 1400, the PSD is significant at frequencies $f = 126$ and 130 Hz, when we see the co-shedding regime is dominant but then changes to a weaker signal at around $f = 100$ Hz between $t^* = 1400$ and 2300, where the reattachment flow regime is stable but has

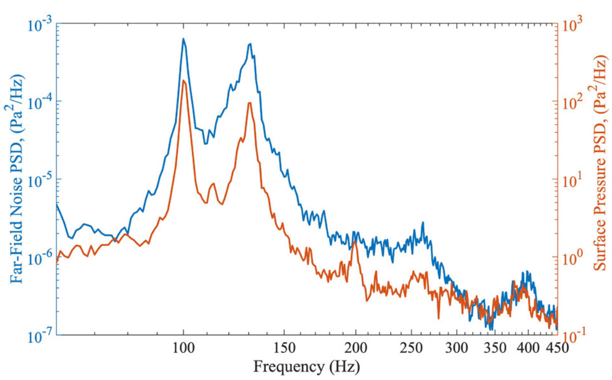

FIG. 4. Power spectral density (PSD) of the fluctuating surface pressure and the far-field acoustic pressure.

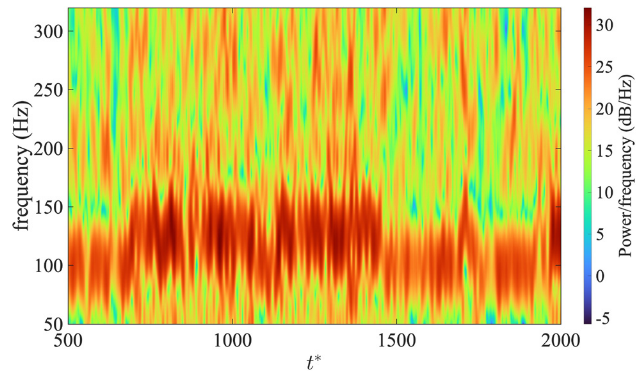

FIG. 5. EPSD for average vorticity along a line in the gap between the two cylinders.

weakened vortex shedding from the second cylinder. Our paper focuses on improving the DMD algorithms used to study the flow features. Regardless, we remain motivated in this venture by the reconciliation of pressure and velocity data and the physical structures relevant to both.

III. A NOVEL APPROACH FOR VORTICITY DATA ANALYSIS USING KEDMD

In this section, we explore the fundamentals of kEDMD when used to analyze our data. We outline the foundations of the algorithm and examine how different kernels influence the results.

A. A brief overview of DMD

DMD[1,3] is a data-driven technique that captures spatial and temporal patterns within modes by using two important $d \times M$ matrices, where d is the total spatial dimension of the data and M is the total number of snapshots. These matrices are traditionally defined as

$$\mathbf{X} = [\underline{X}_1, \underline{X}_2, \ldots, \underline{X}_M], \quad \mathbf{Y} = [\underline{X}_2, \underline{X}_3, \ldots, \underline{X}_{M+1}],$$

where each $\underline{X}_i$ is a vector representing the datafield at the ith snapshot. For our experiment, the PIV window had a grid spacing $\Delta x = 0.814$ mm, with a grid size of 161 x points and 75 y points, thus $d = 12\,075$. Due to the presence of the cylinders, 2289 of these grid-points are not measured. Hence, the dimension of the data can be reduced, or the data can be set to zero at these points. Our experiment took $M = 7800$ snapshots.

We view our data within the context of dynamical systems governed by some potentially nonlinear, unknown function F satisfying

$$\underline{X}_{n+1} = F(\underline{X}_n), \quad n = 0, 1, 2, \ldots. \tag{1}$$

The Koopman operator is a *linear* operator $\mathscr{K}$ acting upon an observable g of the system such that

$$[\mathscr{K} g](\underline{X}_n) = g(\underline{X}_{n+1}). \tag{2}$$

An observable is a function used to measure the state of the system we initially defined in Eq. (1). The goal of DMD[70] is to approximate the Koopman operator by a matrix $\mathbf{K}_{\mathrm{DMD}}$ such that

$$\mathbf{Y} \approx \mathbf{K}_{\mathrm{DMD}}\mathbf{X}. \tag{3}$$

To find this matrix, Exact DMD minimizes Eq. (3) in a least squares sense and defines the Koopman matrix as

$$\mathbf{K}_{\mathrm{DMD}} = \mathbf{Y}\mathbf{X}^{\dagger}, \tag{4}$$

where † denotes the Moore–Penrose pseudo-inverse.

By construction, any eigenfunction of $\mathscr{K}$ should be expected to capture coherent behaviors of the system. In particular, if $\mathscr{K}g = \lambda g$, then

$$g(\underline{X}_n) = \lambda^n g(\underline{X}_0),$$

and hence the eigenvalue λ describes the decay and/or oscillation of the observable g with time. Thus, it is important to approximate potential eigenfunctions by finding the eigenvectors and eigenvalues of the Koopman matrix,

$$\mathbf{K}_{\mathrm{DMD}}\mathbf{V} = \mathbf{V}\Lambda. \tag{5}$$

The matrix $\mathbf{V}$ will contain the modes, and Λ is a diagonal matrix of the corresponding eigenvalues. The entries of this matrix can be related to the eigenfrequencies, given a particular sampling frequency f_s for the data via the relation,

$$f = -i\left(\frac{\log(\lambda) f_s}{2\pi}\right).$$

This experiment used a sampling frequency of $f_s = 1000$ Hz.

When approximating the infinite-dimensional Koopman operator $\mathscr{K}$ by a finite-dimensional linear operator represented by $\mathbf{K}_{\mathrm{DMD}}$, several problems occur:[7] the first is spectral pollution,[71] in which spurious eigenvalues arise that are unrelated to the Koopman operator of the system; the second is the noise corruption of modes,[7,72] where it has been shown that DMD has an inherent bias to any additional random noise as a consequence of solutions to the least squares problem being optimized only when noise is present in $\mathbf{Y}$; finally, the issue we are most interested in is that exact DMD eigenvectors can be considered a linear combination of POD modes, and this linearity can miss spectra associated with nonlinear characteristics of data. This final issue concerns the choice of a *dictionary of basis functions* that we use to derive a Koopman matrix. This dictionary can be considered a finite-dimensional subspace of observables for which the restriction of the Koopman operator acting on this subspace will be approximated by the Koopman matrix $\mathbf{K}_{\mathrm{EDMD}}$. This matrix is the solution to a least squares problem.[65]

The success of EDMD lies in its ability to reflect the inherent nature of the system through a careful choice of dictionary. This will be explored in Sec. III B. More specifically, in EDMD, the Koopman matrix relies on two new matrices Ψ_X and Ψ_Y that are functions of matrices $\mathbf{X}$ and $\mathbf{Y}$. For EDMD with a POD basis, we can calculate

$$\Psi_X = \mathbf{X}^T\mathbf{V}, \quad \Psi_Y = \mathbf{Y}^T\mathbf{V}, \tag{6}$$

where $\mathbf{V}$ is the right singular matrix from a singular value decomposition of the data and T is the usual matrix transpose. Then, we define

$$\mathbf{G} = \Psi_X^*\Psi_X, \quad \mathbf{A} = \Psi_X^*\Psi_Y \tag{7}$$

and define the Koopman matrix $\mathbf{K} = \mathbf{G}^{\dagger}\mathbf{A}$.

To focus on key modes, rank reduction can be performed by truncating the SVD decomposition to restrict attention to $N \leq M$ modes. This will also make the dictionary size N. Naturally, reducing the rank leads to decreased accuracy in the approximation of the system but can help in the presence of noise. A rich dictionary may allow for more intricate features to be better understood. The modal residual is derived in Refs. 62 and 66 as a method of modal error control. The residual of an eigenfunction $\underline{v}$ with eigenvalue λ is used to compute the projection error $\|\mathscr{K}\underline{v} - \lambda\underline{v}\|$ and is defined as

$$\mathrm{res}(\lambda, \underline{v})^2 = \frac{\underline{v}^*\left(\mathbf{L} - \lambda\mathbf{A}^* - \bar{\lambda}\mathbf{A} + |\lambda|^2\mathbf{G}\right)\underline{v}}{\underline{v}^*\mathbf{G}\underline{v}.} \tag{8}$$

This formula relies on an additional matrix

$$\mathbf{L} = \Psi_Y^*\Psi_Y. \tag{9}$$

Calculating the projection error of a mode helps avoid spurious eigenvalues. This notion will be considered in more detail during Sec. III B when we compare the effects of dictionary choices more directly. We use the residual as a means to measure modal reliability as opposed to modal modulus since it has been demonstrated in previous work, such as Ref. 62, that it is a more accurate indicator of convergence to true dynamics. In this paper, an example showed that recreating a system with the lowest residual modes can give more accurate results than with the modes closest to the unit circle. We prefer the residual to modal energy since there is no guarantee that high-energy modes are reliable solely due to their importance in modal reconstruction. If the algorithm does not capture the system well enough, it may feature high-energy spurious modes that may be misleading. The role of the residual is to assess whether a potential eigenpair (λ, v) is accurate by approximating its relative residual

$$\frac{||(\mathscr{K} - \lambda I)v||}{||v||}, \tag{10}$$

which is well approximated by Eq. (8), since

$$\lim_{M\to\infty}[\Psi_X^*\mathscr{K}\Psi_Y]_{jk} = \langle\psi_j, \mathscr{K}\psi_k\rangle,$$

and similar results hold for combinations including Ψ_Y (as explained in Sec. 3 of Ref. 62).

In Ref. 62, the use of *training data* is discussed as an additional method to improve modal accuracy. Here, an additional independent dataset is used to construct the dictionary and facilitates the implementation of convergence theorems for eigenvalues. An alternative approach that does not require additional data is discussed in Ref. 63, in which a dual least squares problem is considered. For our experiment, the large number of snapshots is suitable for the former approach, and we separate the dataset of length M into two separate segments of length M_1 and M_2, respectively. The former is the training data used for the dictionary, and the latter is the data we aim to approximate with our algorithms.

The final important definition is the *kernel* used to form a dictionary. We have mentioned that EDMD introduces a nonlinear dictionary via matrices $\Psi_{X,Y}$; however, the first algorithm to directly relate functional kernels to dictionary choices was *kernelized* EDMD (kEDMD).[61] For this algorithm, one explicitly chooses a kernel function $\mathscr{S}(\underline{x}, \underline{x}')$ and defines preliminary matrices $\tilde{\mathbf{G}}$, $\tilde{\mathbf{A}}$, $\tilde{\mathbf{L}}$ such that

$$\tilde{\mathbf{G}}_{ij} = \mathscr{S}(\underline{X}_i, \underline{X}_j), \quad \tilde{\mathbf{A}}_{ij} = \mathscr{S}(\underline{X}_i, \underline{Y}_j), \quad \tilde{\mathbf{L}}_{ij} = \mathscr{S}(\underline{Y}_i, \underline{Y}_j). \tag{11}$$

With these matrices, one computes the eigendecomposition

$$\tilde{\mathbf{G}} = \mathbf{Q}\Sigma^2\mathbf{Q}^* \tag{12}$$

and defines truncated matrices

$$\tilde{\mathbf{Q}} := \mathbf{Q}(:, 1:N),$$
$$\tilde{\Sigma} := \Sigma(1:N, 1:N).$$

Then, the (compressed) kEDMD Koopman matrix is

$$\tilde{\mathbf{K}} = \left(\tilde{\Sigma}^{\dagger}\tilde{\mathbf{Q}}^*\right)\tilde{\mathbf{A}}\left(\tilde{\mathbf{Q}}\tilde{\Sigma}^{\dagger}\right). \tag{13}$$

The analogous matrices $\Psi_{X,Y}$ to Eq. (6), which we denote $\Psi^k_{X,Y}$ for this algorithm, are

$$\Psi^k_X = \tilde{\mathbf{G}}^{\dagger}\left(\tilde{\mathbf{Q}}\tilde{\Sigma}^{\dagger}\right), \quad \Psi^k_Y = \tilde{\mathbf{A}}\left(\tilde{\mathbf{Q}}\tilde{\Sigma}^{\dagger}\right). \tag{14}$$

We can calculate the residual of a kEDMD mode via an equivalent definition to Eq. (8)

$$\mathrm{res}(\lambda, \underline{v})^2 = \frac{\underline{v}^*\left(\tilde{\mathbf{L}} - \lambda\tilde{\mathbf{A}}^* - \bar{\lambda}\tilde{\mathbf{A}} + |\lambda|^2\tilde{\mathbf{G}}\right)\underline{v}}{\underline{v}^*\tilde{\mathbf{G}}\underline{v}}. \tag{15}$$

For this paper, we will investigate four common choices of kernels

$$\mathscr{S}^{\mathrm{Lin}}\left(\underline{x}, \underline{x}'\right) := \underline{x}'\underline{x}, \tag{16a}$$
$$\mathscr{S}^{\mathrm{Lap}}\left(\underline{x}, \underline{x}'\right) := \exp\left(-\|\underline{x} - \underline{x}'\|/c\right), \tag{16b}$$
$$\mathscr{S}^{\mathrm{G}}\left(\underline{x}, \underline{x}'\right) := \exp\left(-\|\underline{x} - \underline{x}'\|^2/\tilde{c}^2\right), \tag{16c}$$
$$\mathscr{S}^{\mathrm{p},n}\left(\underline{x}, \underline{x}'\right) := \left(1 + \underline{x}'^*\underline{x}/c^2\right)^n. \tag{16d}$$

Equation (16a) is for a linear kernel where the dictionary consists of linear modes. Equation (16b) is for a Laplacian kernel. Equation (16c) is for a Gaussian kernel, while the final kernel in Eq. (16d) is for an nth degree *polynomial* kernel. Here, c is the average l_2-norm of the mean-subtracted snapshot, while $\tilde{c}$ is the average of the snapshot *without* subtracting the mean. A preliminary investigation of our dataset demonstrated that a good choice for the polynomial kernel was a quartic polynomial kernel, and we separately observed that an octic polynomial produced characteristics very similar to the quartic, but with slightly lower residual. We omit comparisons on polynomial kernels for brevity, but we believe optimizing based on the underlying theory will be possible in the future. Laplacian and Gaussian kernels are popular choices due to their ability to successfully capture nonlinearities in data, since they are universal approximators.

B. A low-rank exploration of velocity modes

To explore the key modes expected from kEDMD, we fix $N = 30$ and produce a low-rank data decomposition.

For now, we focus more on what flow features we can uncover using multiple kernels. In Sec. IV, we will compare modes using different kernels. We fix $M_1 = M_2 = 3900$ and divide our data into training and experimental sets to perform kResDMD.

Vorticity, being a first-order quantity with complex dynamics and steep gradients, makes low-rank DMD approximations less effective at capturing a broad range of behaviors. This is demonstrated in Fig. 6 in which we plot the spectrum for the linear kernel, where only a few frequencies lie near the unit circle, representing modes that capture physical phenomenon more reliably. We will see in future examples that these modes represent the two shedding frequencies and their first harmonics as well as steady-state behavior near $\lambda = 1$. Therefore, we instead choose to perform DMD on *both* velocity fields, that is

$$\mathbf{X} = [\mathbf{U}; \mathbf{V}].$$

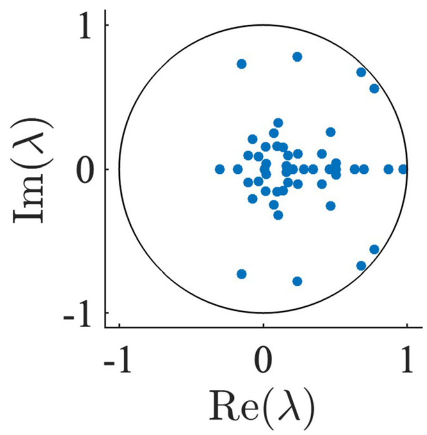

FIG. 6. Spectrum for the low-rank velocity eigenvalues. The unit circle $|\lambda|$ is indicated in black.

Modes are then projected onto the vorticity field by plotting Koopman modes. Vorticity inherently relies on velocity fields; hence, we expect important behaviors and frequencies to be captured using this method. We will see that these modes are very similar to those obtained when using vorticity directly. However, this section's exploration is mostly motivational for the final sections, where we will increase N and use the vorticity field to capture intricate flow features directly associated with the vorticity.

A brief comparison of the plots in Fig. 7 shows that the eigenvalues of nonlinear kernels tend to be close to the unit circle, suggesting they capture more persistent flow features. There are subtle nuances to the individual nonlinear kernels. The quartic kernel captures an extra mode at around $\lambda = i$ but remains relatively similar to the Laplacian results. Conversely, the Gaussian kernel also captures more low-frequency modes near $\lambda = 1$ but with a non-zero imaginary part.

To view specific modes, we divide our attention between the steady dynamics ($\lambda = 1$), modes and harmonics related to the first shedding frequency, and modes and harmonics related to the second shedding frequency.

1. Steady dynamics

The steady flow features are captured at $\lambda \approx 1$. The linear kernel has several modes with $\Im[\lambda] = 0$; however, their low eigenvalue modulus suggests they are less reliable. For measure-preserving systems, the residual of a mode is related to the modulus of a mode via $\mathrm{res} \approx \sqrt{1 - |\lambda|^2}$, as discussed in Ref. 64. This approximation holds well for the low-rank approximation of the system. We will focus on the two modes of the Laplacian kernel with $\lambda \approx 1$.

Our first projected Koopman modes are plotted in Fig. 8. From this point onward, we only plot dimensional vorticity modes which will all have units s^{-1}. The first mode in Fig. 8(a) is a high-energy

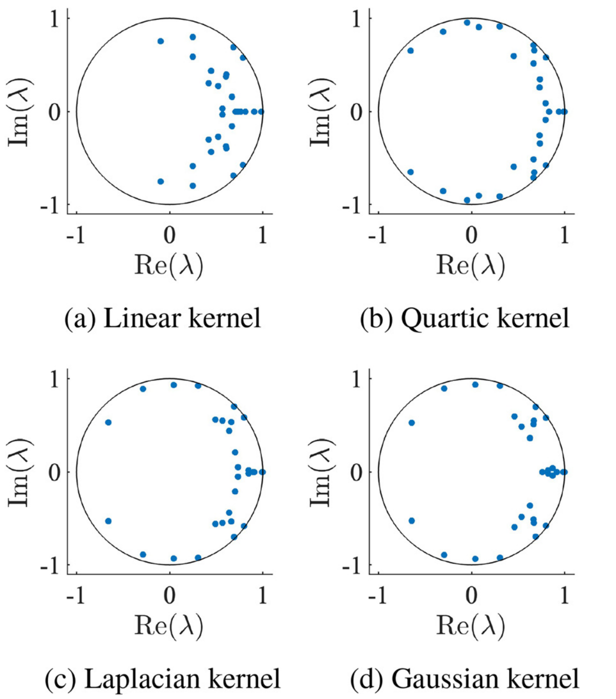

FIG. 7. Eigenpairs for the low-rank velocity eigenvalues.

steady-state mode found within the spectra of all kernels. This mode is similar to the lowest frequency mode computed by an alternative algorithm, recursive DMD, in Figs. 18(a), 20(a), and 22(a) of Ref. 47. We see important features related to each of the two regimes: the shedding of vortices in the gap related to the co-shedding regime and the formation and attachment of large shear layers between the two cylinders that is seen in the reattachment regime. However, the mode has far less energy in the wake of the downstream cylinder.

The second mode is closer to $\lambda = 1$ and is unique to the nonlinear kernels. These modes may be linked to more intricate nonlinear flow features, such as shear layer instabilities and more complex vortex dynamics. This mode could be more relevant to the inherent bistability of the flow.

2. The first shedding frequency

In Fig. 9(a), the most significant peak for both the far-field noise and the surface pressure is found at 100 Hz. This shedding frequency

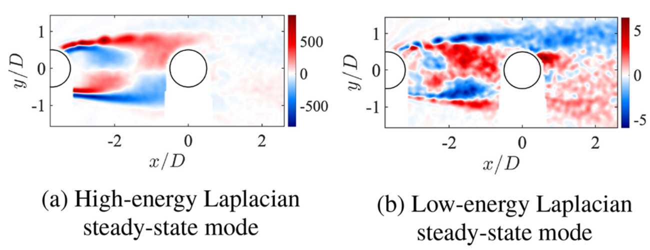

FIG. 8. Steady-state low-rank Koopman modes projected onto vorticity data using the Laplacian kernel. Modes are dimensional with units s^{-1}.

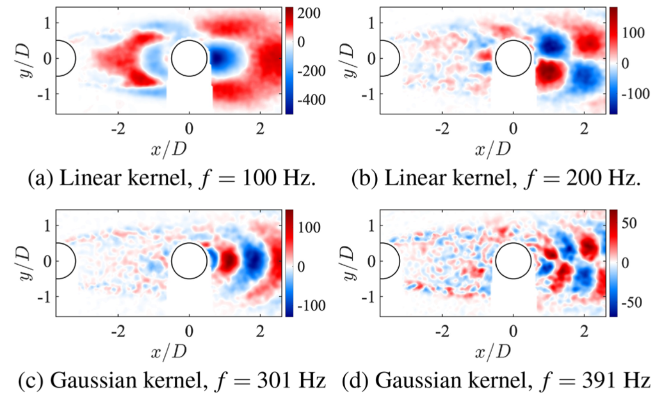

FIG. 9. Low-rank Koopman modes for the first shedding frequency and its harmonics projected onto vorticity data.

is associated with the reattachment regime. The mode corresponding to the primary vortex frequency in Fig. 9(a) features shedding structures in the upstream cylinder wake that are deflected by the downstream cylinder. We also see separated shear layers that reattach to the leeward side of the downstream cylinder.

In Fig. 9(b), we plot the first harmonic frequency for the primary vortex shedding frequency. This mode shows smaller-scale structures being shed from the downstream cylinder. The higher frequency dynamics captured by this mode highlights the presence of secondary shear layer instabilities in the wake of the second cylinder, which influence the overall wake structure. There is significantly less activity in the gap, reflecting the lack of vortex shedding in the gap within this regime. This feature resembles the third and fourth harmonic modes in Figs. 9(c) and 9(d). The linear kernel cannot pick out any high-frequency modes, so we used the Gaussian kernel. All nonlinear kernels demonstrate the shedding of several clearly defined elongated structures that dominate the flow. For Fig. 9(d), these structures are less defined and have as much energy as the smaller structures in the gap between cylinders. This could imply that the downstream cylinder stabilizes the overall flow pattern, with the chaotic structures in the gap serving to dissipate energy before the flow reorganizes into larger vortices. These longer structures likely correspond to vortex formation and shedding in the wake of the second cylinder, driven by interactions with the incoming disturbed wake from the first cylinder.

3. The second shedding frequency

The secondary shedding mode in Fig. 10(a) shows separated shear layers that form vortex shedding structures within the gap between the two cylinders and contribute to significant vortex shedding by the downstream cylinder. These features correspond to the co-shedding regime. Figure 4 shows several peaks around the second shedding frequency. With a low-rank dictionary, it is hard for even the nonlinear kernels to pick out all separate phenomena, but they can pick out several relevant harmonics. We show the first harmonic from the Laplacian kernel of an earlier peak in Fig. 10(b) and the first harmonic for (approximately) the second shedding frequency from the quartic polynomial kernel in Fig. 10(c). These modes have similar characteristics but more refined structures in the wake of the second cylinder or the gap between cylinders for each respective figure. Here,

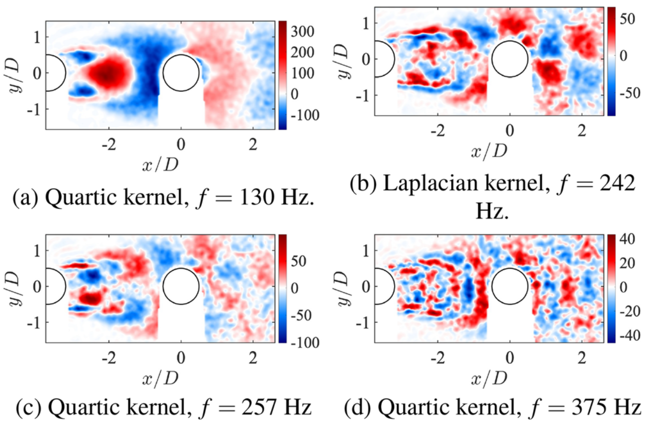

(a) Quartic kernel, $f = 130$ Hz. (b) Laplacian kernel, $f = 242$ Hz. (c) Quartic kernel, $f = 257$ Hz (d) Quartic kernel, $f = 375$ Hz

FIG. 10. Low-rank Koopman modes for the second shedding frequency and its harmonics projected onto vorticity data.

the shear layers merge to form vortical structures in the gap that interact with the downstream cylinder. The larger structures initially pass over the cylinder but break into smaller ones as the flow transitions to a more turbulent state.

Finally, a high-frequency mode captured successfully by the quartic kernel is shown in Fig. 10(d). Unlike Figs. 10(b) and 10(c), this mode has symmetry about $y = 0$ and a more even spread of energy between the gap and the wake. The breakup of thin shear layers within the gap suggests this mode may contribute to the transition from the reattachment regime to the co-shedding regime.

To finish this section and motivate the next, we visually represent how the four kernels differ at $N = 30$. We overlay the modes that each kernel calculated and their residuals [see Eq. (8)] alongside the far-field noise PSD in Fig. 11. This plot excludes the steady-state modes, and we plot $1/\mathrm{res}$ so more reliable modes align better with the larger (more important) peaks in the PSD they represent. The nonlinear kernels all have lower residuals for the harmonic frequencies and cover a broader range of frequencies.

IV. COMPARING NONLINEAR KERNELS

Now that we have discussed the experimental motivation extensively, and we focus on the impact of dictionary choice on results. We

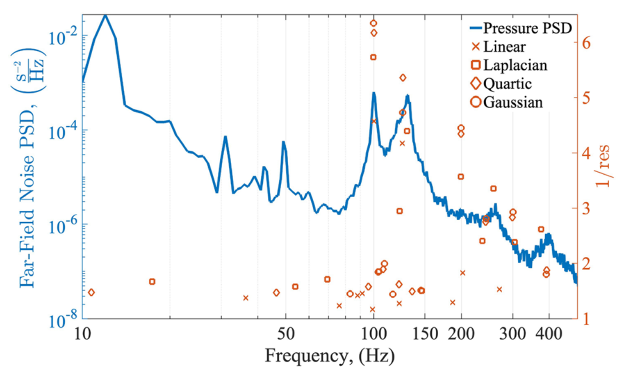

FIG. 11. Low-rank velocity eigenvalues and their associated $1/\mathrm{res}$ value plotted against the far-field noise PSD.

will compare kernels for certain nonlinear dictionaries Eqs. (16b)–(16d) in their performance against the linear dictionary Eq. (16a) with two larger dictionary sizes (N). We have already observed that nonlinear dictionaries have an advantage over a linear dictionary in capturing a wider range of modal frequencies and lower residuals, but this was for the simplistic low-rank case. We will now focus only on the vorticity data calculated from the experimentally measured **U** and **V** fields. Although we anticipate some difficulties with the modal decomposition of the vorticity data, a larger dictionary size captures more of the intricacies of the flow more accurately.

A. The impact of dictionaries on residuals and spectra

We compute the Koopman matrix for each algorithm to find all modes and residuals to visualize the approximated spectrum. The first important concept that we will compare is modal energy, defined as

$$\mathrm{En} = \frac{\|\Psi_X \, \underline{v}\|}{\sqrt{M_2}}. \tag{17}$$

We will represent individual modal energy as a percentage of the total DMD modal energy. Energy can be used to rank or prioritize modes. The second important quantity is the *residual* of a mode, defined in Eq. (8) or equivalently as

$$\mathrm{res}(\lambda, \underline{v}) = \frac{\|\Psi_Y^k \underline{v} - \lambda \Psi_X^k \underline{v}\|}{\|\Psi_X^k \underline{v}\|}. \tag{18}$$

In addition, we calculate pseudospectra[62,66] to demonstrate the stability or instability of spectra. That is, for any candidate point z in the complex plane, we calculate

$$\tau(z) = \min_{\underline{v} \in \mathbb{C}^N} \mathrm{res}(z, \Psi \underline{v}). \tag{19}$$

Here, we use the shorthand notation $\Psi \underline{v}$ to refer to the summation

$$\Psi \underline{v} = \sum_{j=1}^{N} \psi_j(\underline{x}) v_j,$$

where each ψ_j is a member of the kernelized dictionary. The pseudospectrum is another important method for detecting spurious eigenvalues unrelated to the spectrum of the Koopman operator and, thus, serves as a means of error control. For every point in the complex λ-plane, the pseudospectrum associates a value ε. This value determines how large a perturbation of the operator needs to be for λ to be in its spectrum. In summary, the pseudospectrum with associated value ε is the region of the complex plane corresponding to spectra of perturbations of the underlying Koopman operator $\mathscr{K}$ of size ε.

1. N=1000

Our first choice of dictionary size is $N = 1000$. This represents a mid-rank approximation in which we sacrifice some numerical efficiency to capture more low-residual modes representing a larger selection of flow features.

First, in Fig. 12, we plot the eigenpairs for each method. The residuals are indicated by color, and some important modes are captured with low residuals nearer to the unit circle. The distinction between linear and nonlinear kernels is noticeable. First, all nonlinear kernels have more nonspurious eigenvalues and tend to spread out

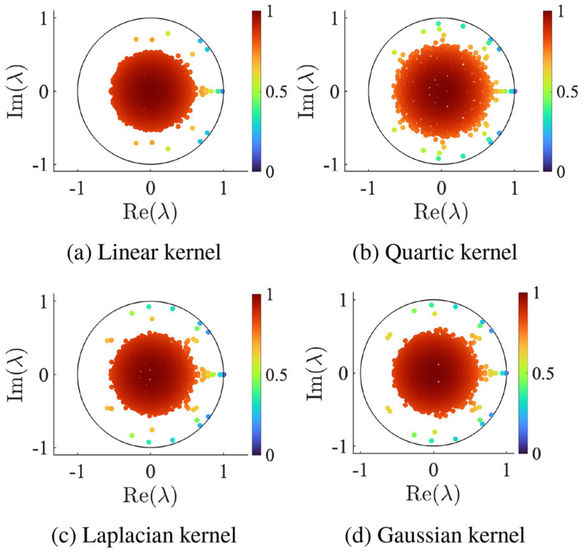

FIG. 12. Eigenpairs and residuals for the mid-rank case. The unit circle $|\lambda|$ is indicated in black, and the mode color represents residual.

more from the origin. We see that the quartic kernel has the most spread out eigenvalues. However, not all of these modes may be reliable. The Laplacian and Gaussian kernels appear quite similar, and Figs. 12(c) and 12(d) differ only in terms of residuals, with the Gaussian kernel having slightly lower residuals for the high-frequency modes near $\lambda = -1$ and some of the more transient modes between the unit circle and central region of spectral pollution.

We plot pseudospectra in Fig. 13 to support our kernel comparisons. The high-frequency effects are harder to capture, but the spread in the darker region toward $\lambda = -1$ seen in Fig. 13(d) shows that a

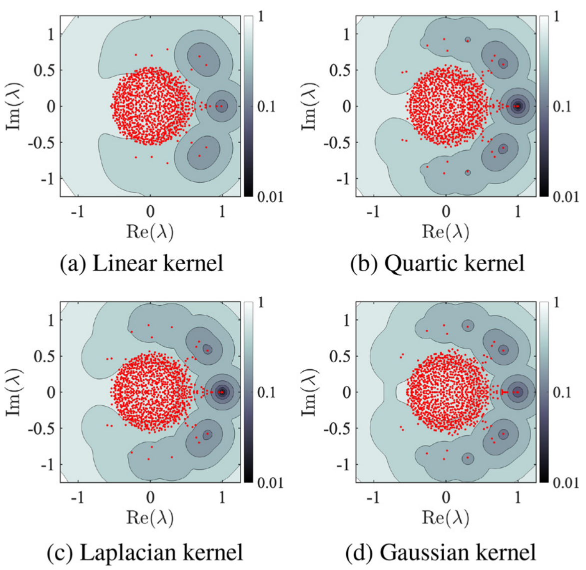

FIG. 13. Pseudospectra [Eq. (19)] for linear and nonlinear dictionaries for the mid-rank case. Eigenvalues from Fig. 12 are indicated in red.

careful choice of the kernel can provide insight into the flow. Small regions surrounding key modes become more pronounced for the nonlinear kernels, suggesting they capture coherent structures better within these modes with a rank $N < M_2$.

Finally, we discuss the energies of each mode, including the modal frequency and residual. As mentioned in the introduction, ResDMD is unique as a DMD method in that it uses the residual as a ranking criterion for modal importance. In contrast, other methods, such as Exact DMD and SPOD, focus on modal energy or modal modulus.

To demonstrate the importance of the distinction between energy and residual, we plot energy-frequency modal comparisons for the $N = 1000$ case. Since we now have more spurious modes, we restrict our attention to modes that satisfy res < 0.8. This value is chosen for esthetic purposes to remove a significant amount of spectral pollution. The bulk of modes for each method are around this value except for the quartic kernel. It is clear from Fig. 14(a) that the residual is a better criterion for modal ranking since we see that a low-residual mode for the second shedding frequency has less energy than five spurious modes. Conversely, each nonlinear kernel exhibits a trend where the more energetic modes also correspond to the low-residual modes, suggesting that these kernels prioritize energy distribution to more reliable modes. Additionally, we observe that each nonlinear kernel assigns more similar energy content to the key shedding modes. Furthermore, we note that the nonlinear kernels have more spurious modes, as their average residual is lower in every case.

If we perform a low-rank approximation, such as Fig. 6, all algorithms struggle to produce a mode at around 130 Hz for the second shedding frequency. This is due to several distinct peaks between 120 and 130 Hz that the low-rank algorithms struggle to distinguish. Once we set $N = 1000$, all four methods correctly approximate the second shedding frequency. In addition, smaller secondary peaks in the pressure power spectra in Fig. 3 are now represented by several nonspurious modes in Figs. 14(b)–14(d).

2. N=3000

Next, we choose a high-rank approximation with a dictionary size of $N = 3000$. Since our data contain $M_2 = 3900$ snapshots, we are approaching the limit in which we can capture more of a continuous spectrum. However, such a limit is still a finite discrimination of this spectrum that may be hindered by overfitting and has a high computational cost; thus, there are no guarantees that this spectrum is the exact continuous Koopman spectrum. Thus, it is worth investigating how beneficial a high rank can be. In particular, for some experiments with a larger number of snapshots, a full-rank approximation becomes impractical.

We plot the eigenvalues and residuals for the high-rank approximation in Fig. 15.

In the large N limit, we still see some spectral pollution, but a clearer disk of modes emerges that may be approximating a continuous spectrum. However, for the nonlinear kernels, it is possible to spot several separate nonspurious modes that relate to the shedding frequencies and their harmonics.

We show updated high-rank pseudospectra in Fig. 16. We observe an annulus that approaches the unit circle with a region representative of spectral pollution at its center. Moreover, exceptionally low-residual modes (with a residual less than 0.4, a baseline chosen to

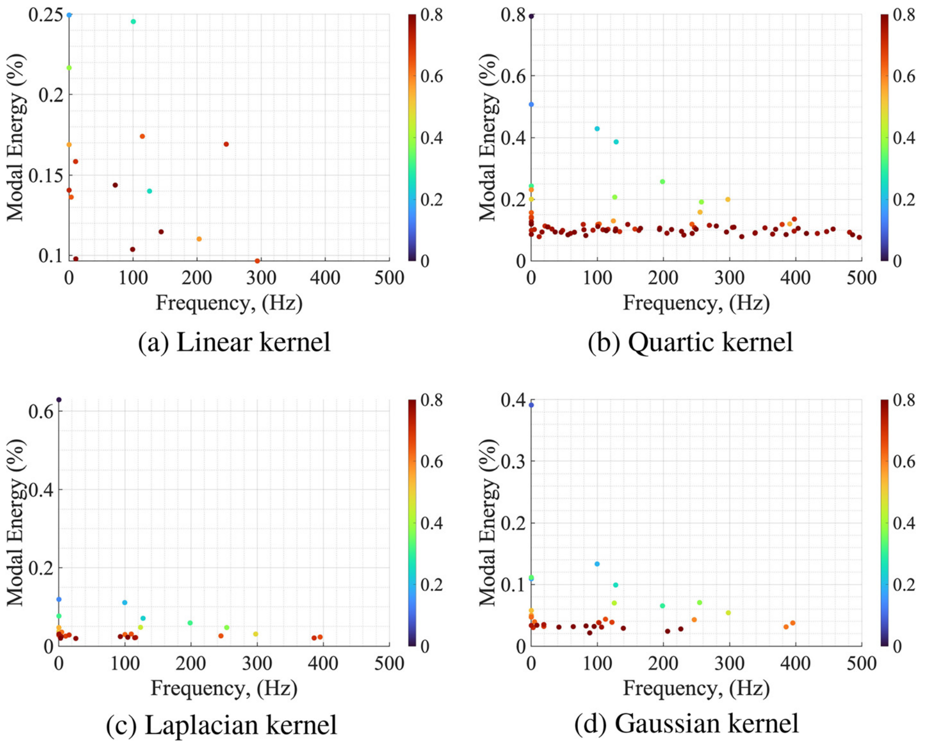

FIG. 14. Modal energy [Eq. (17)] against modal frequency with residual [Eq. (8)] indicated by color for the mid-rank case. Only modes satisfying res < 0.8 are kept.

exclude the annular region) are highlighted in green and demonstrate the superiority of the nonlinear kernels. Any kEDMD exploration of experimental data is improved by initially exploring the pseudospectrum using the ResDMD algorithm, as it demonstrates what regions of the spectra are the most significant and enables a simple ranking of them.

Finally, we explore the energy distribution for this high-rank approximation. We focus on the first 300 modes with the lowest residual to avoid less reliable modes that may not contain significant or accurate flow structures. We see that the higher residual modes that can be attributed to transient effects carry the least amount of energy.

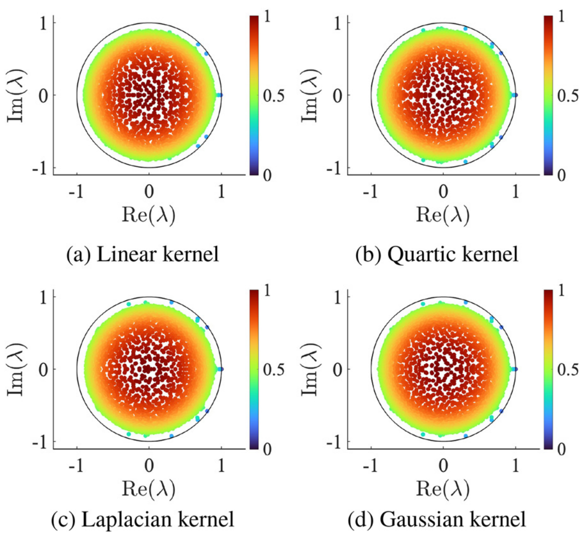

FIG. 15. Eigenpairs and residuals for the high-rank case. The unit circle $|\lambda|$ is indicated in black, and the mode color represents residual.

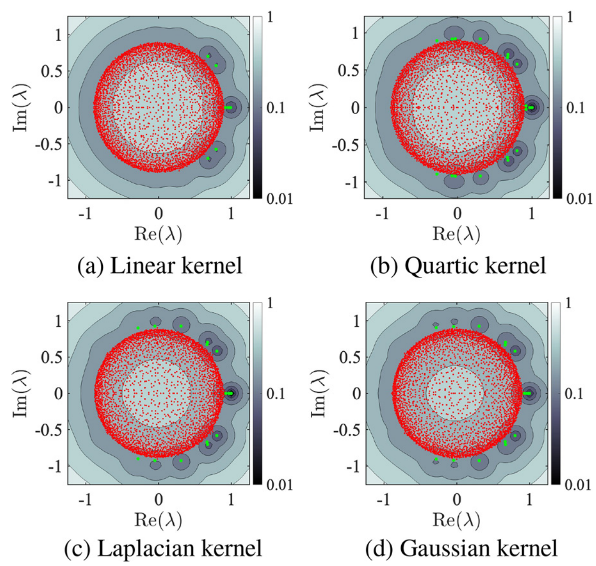

FIG. 16. High-rank pseudospectra [Eq. (19)] for linear and several nonlinear dictionaries. Eigenvalues from Fig. 15 are indicated in red with modes satisfying res < 0.4 indicated in green.

When comparing the four kernels for this case, we notice some differences compared with Fig. 14. First, the high-energy mode at $\lambda = 1$ is now more dominant within the quartic kernel spectrum than the other two nonlinear kernels. When viewing the residuals closely, we can see that the nonlinear kernels offer double the number of key nonspurious modes to investigate. A Koopman mode is considered nonspurious if it corresponds to a physically meaningful, dynamically persistent structure in the system's evolution. These modes represent key physical features of the flow captured accurately by the modal decomposition method and will be the focus of Sec. IV B. Moreover, the Laplacian kernel has a less consistent energy distribution, with a steady-state mode carrying around 4.8% of the total energy [represented with a break in the y-axis in Fig. 17(c)]. This suggests the Laplacian kernel may not be suitable for data predictions or reconstructions that involve transient effects since the steady-state dynamics captures a larger proportion of modal energy.

B. High-rank vorticity modes

To finish this section, we review some modal comparisons for the $N = 3000$ case. This time, we emphasize the modal residual since this indicates how well the modes approximate an eigenfunction of the Koopman operator.

While we can learn plenty from the two primary modes, there are other features captured across other frequencies that we wish to investigate. Here, dictionary choice helps to ensure that lower residual modes are chosen at the most accurate frequencies. Since we can only approximate the full spectrum with a finite number of modes, we are restricted to what modes the algorithm computes successfully at lower residuals. Hence, when we plot our mode comparisons, we also include the specific frequency and residual captured by the algorithm.

We present five modes; three are revisited from Sec. III B 2, while two distinct frequencies are introduced that are related to previously studied modes.

The first mode is a low-frequency mode with relatively low residual, but the mode itself does not lie at $\lambda \approx 1$. These modes show high-energy shear layers that breakup into less energetic regions above the downward cylinder, best represented by the quartic kernel [Fig. 18(b)], which has the lowest residual of the four kernels. The differences in residual seem very small, but the results indicate that the sensitivity of the results on this parameter may be rather significant. The nonlinear kernels are similar to the steady-state modes in Fig. 8 within the gap.

The second mode we consider relates to the second shedding frequency at $f = 130\,\text{Hz}$ associated with the proceeding smaller peaks from Fig. 4. These earlier peaks may relate to different shedding phenomena as the flow transitions from one state to another. We see in Fig. 19 that all four modes are similar. However, the nonlinear modes have a much lower residual and demonstrate clearer vortex shedding from the downstream cylinder that is similar to Fig. 9(a). The primary difference between these earlier peaks and the mode in Fig. 9(a) is the longer, thinner shear layers that indicate there may be some influence from the transition between regimes.

For the third mode, we fix $f \approx 199\,\text{Hz}$ and compare the second harmonic of the first shedding frequency to Fig. 9(b). All these modes have low residuals and are very similar. The structures shed by the second cylinder are less even than in the previous modal approximation. This supports the previous hypothesis that a modal decomposition of the vorticity field should provide more accuracy of the structures we

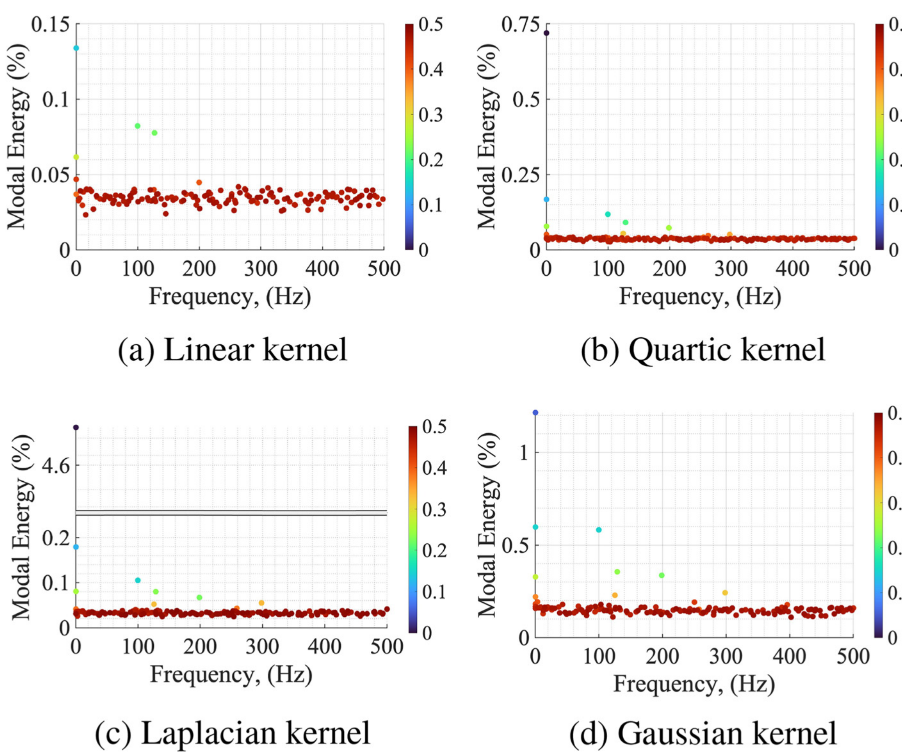

FIG. 17. Modal energy [Eq. (17)] against modal frequency with residual [Eq. (18)] indicated by color for the high-rank case. Only modes with residual within the top 10% are kept.

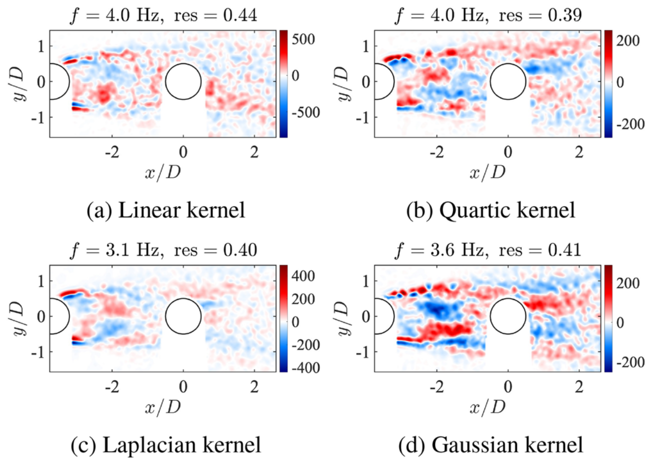

FIG. 18. High-rank modal comparison for a low-frequency mode at ≈ 4 Hz.

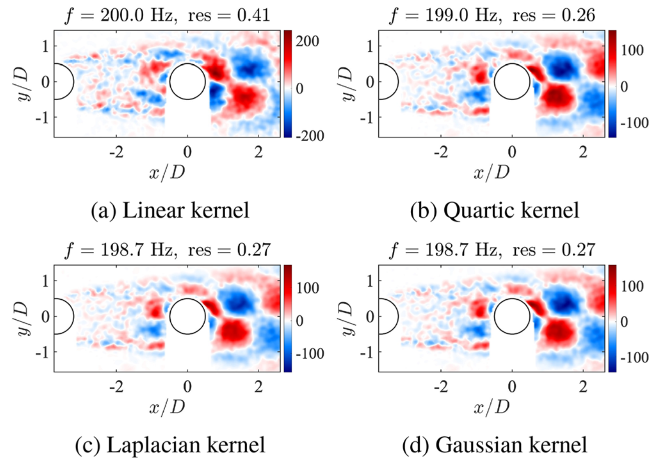

FIG. 20. High-rank modal comparison for the first harmonic to the first shedding frequency at ≈ 199 Hz.

see when compared to projections of velocity modes. The higher residual for Fig. 20(a) could be associated with a less accurate portrayal of the mode in the gap between the two cylinders, and the higher magnitude of structures shed from the downstream cylinder. This is a feature that remains very consistent among the nonlinear kernels.

Our fourth mode is representative of a second harmonic related to the second shedding frequency, comparable to Figs. 9(b) and 9(c). All modes show similarity in the wake of the second cylinder but differ in their strength and structures in the wake of the first. The clearer and more defined structures are found in Fig. 21(c), which supports the importance of the residual when compared with the linear kernel in Fig. 21(a).

The final frequency is the third harmonic of the first shedding frequency. In Fig. 22, the visual differences between the linear and nonlinear kernels are pronounced. As in Fig. 21, this supports using residuals to ascertain whether modes will give clear and suitable results.

V. KERNELIZED RIGGED DMD: AN ALGORITHM FOR GENERALIZED EIGENVECTORS

The previous sections highlight the importance of a nonlinear dictionary in kEDMD. In addition, the physical motivation is to find an explicit connection between coherent structures in vorticity modes and peaks observed in the far-field noise PSD. A particular weakness observed for kEDMD was its restriction to eigenvalues of a Koopman matrix that forms a finite-dimensional approximation of the Koopman operator. A novel algorithm, Rigged DMD, was constructed to overcome this weakness in Ref. 12.

Rigged DMD computes generalized eigenfunction decompositions of Koopman operators. It implements another algorithm, measure-preserving EDMD (mpEDMD),[73] which approximates the Koopman operator as a finite-dimensional unitary matrix that preserves the systems norm so that all modes satisfy $|\lambda| = 1$. Then, the resolvent of this operator is sampled *at a specific frequency* to form a

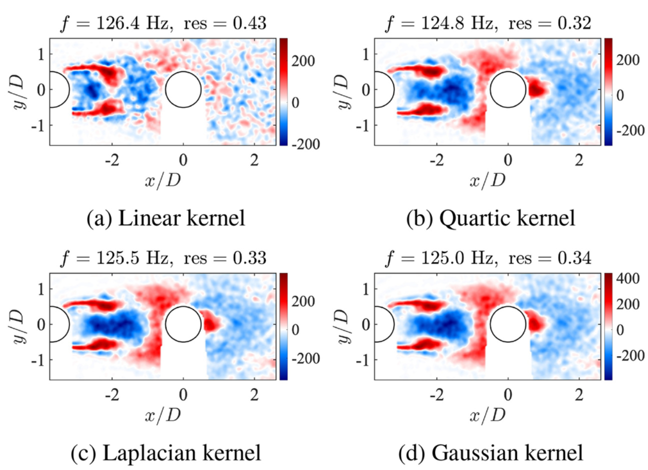

FIG. 19. High-rank modal comparison near the second shedding frequency at ≈ 125 Hz.

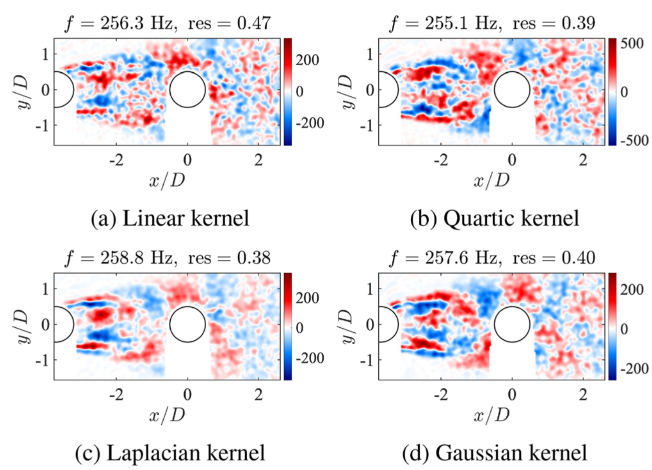

FIG. 21. High-rank modal comparison for the first harmonic to the second shedding frequency at ≈ 256 Hz.

smoothed approximation of the generalized eigenfunction, using user-determined smoothing parameters for a wavepacket approximation.

For completeness, we reproduce the traditional Rigged DMD algorithm from Ref. 12 in Algorithm 1. Algorithm 2, taken from Ref. 12, can be used for the post-processing of generalized eigenfunctions. Like resDMD, several convergence theorems accompany this algorithm and guarantee the accuracy for these generalized eigenfunctions and spectral measures.

In Ref. 12, several physical examples are presented that showcase Rigged DMD. For this paper, in keeping with the focus of Sec. IV, we use Rigged DMD to analyze our experimental data, focusing on exploring the effects of dictionary choice. That is, we will introduce a novel algorithm, kernelized Rigged DMD (kRigged DMD), to compare alongside "standard" Rigged DMD and investigate the impact of the initial choice of dictionary on both the spectral measure and the generalized eigenfunctions for key frequencies. For clarity, we outline our novel updated algorithm to approximate spectral measures and eigenfunctions in Algorithm 3.

A. Coherent structures and noise

One way we can utilize the advantages of kRigged DMD within our experimental analysis is to investigate the *spectral measure* of our vorticity data. The spectral measure can be seen as an alternative to the power spectral density that removes windowing and broadening effects. It is closer to the continuous limit of the fast Fourier transform.

In this section, we show the promise of a modal approach to identifying coherent flow structures to which tonal far-field noise seen in Fig. 4 can potentially be attributed. A novel approach to identifying structures relevant to specific peaks at the pressure spectrum is to plot the spectral measure of vorticity signals together with the far-field noise pressure spectra and see which peaks may overlap. We demonstrate this in Fig. 23(a) for the vorticity signal at a point in the gap between the two cylinders, where we expect the first shedding frequency to dominate. Then, in Fig. 23(b), we show the spectral measure for the vorticity signal at a point in the wake of the second cylinder, where the second shedding frequency should dominate. We fix the

ALGORITHM 1. The Rigged DMD algorithm [12] for computing generalized eigenfunctions of $\mathcal{K}$.

Input: Snapshots $\mathbf{X}$, $\mathbf{Y}$, quadrature weights $\{w_m\}_{m=1}^{M}$, dictionary of observables $\{\psi_j\}_{j=1}^{N}$, $\{a_j\}_{j=1}^{m}$ with $\mathrm{Im}(a_j) > 0$, smoothing parameter $\varepsilon > 0$, angles for the spectral measure $\Theta_1 \subset [-\pi, \pi]_{\mathrm{per}}$, angles $\Theta_2 \subset [-\pi, \pi]_{\mathrm{per}}$ to calculate generalized eigenfunctions, observable g for the spectral measure and observables $\mathbf{g} = [g_1, \ldots, g_l]^T$ used to calculate generalized eigenfunctions.

Stage A: Build discretizations of $\mathcal{K}$ and g.

1: Apply mpEDMD [73] to compute $\mathbf{K}$, $\mathbf{V}$ (eigenvectors), Λ (eigenvalues).

2: Compute the vector $\mathbf{g} = (\mathbf{W}^{1/2}\Psi_X\mathbf{V})^{\dagger}\mathbf{W}^{1/2}(g(\underline{X}^{(1)}), \ldots, g(\underline{X}^{(M)}))^{\top}$.

Stage B: Apply Rigged DMD to build wave-packed approximations.

1: Solve the $m \times m$ system from Stage A for the residues $\alpha_1, \ldots, \alpha_m \in \mathbb{C}$.

2: For each $\theta \in \Theta$ and $j = 1, \ldots, m$, compute

$$\mathbf{g}_\theta^{(j,+)} = (\Lambda + e^{i\theta - i\varepsilon a_j})(\Lambda - e^{i\theta - i\varepsilon a_j})^{-1}\mathbf{g}, \quad \mathbf{g}_\theta^{(j,-)} = (\Lambda + e^{i\theta - i\varepsilon \bar{a}_j})(\Lambda - e^{i\theta - i\varepsilon \bar{a}_j})^{-1}\mathbf{g}.$$

(NB: No matrix multiplications or inverses are needed in this step since Λ is diagonal.)

3: For each $\theta \in \Theta$, compute

$$\tilde{\mathbf{g}}_\theta = \frac{-1}{4\pi}\sum_{j=1}^{m}(\alpha_j\mathbf{g}_\theta^{(j,+)} - \bar{\alpha}_j\mathbf{g}_\theta^{(j,-)}) \in \mathbb{C}^N \quad \text{(mpEDMD eigenvector coordinates)},$$

$$\mathbf{g}_\theta = \mathbf{V}\tilde{\mathbf{g}}_\theta \in \mathbb{C}^N \quad \text{(original dictionary coordinates)}.$$

4: For the spectral measure at each $\theta \in \Theta$, compute

$$\xi(\theta) = \tfrac{-1}{2\pi}\sum_{j=1}^{m}\mathrm{Re}(\alpha_j\mathbf{g}^*\mathbf{g}_\theta^{(j,+)}) \in \mathbb{R}.$$

Output: Vectors $\{\mathbf{g}_\theta : \theta \in \Theta\}$ such that each $\Psi\mathbf{g}_\theta \in L^2(\Omega, \omega)$ is a wave-packet approximation to a generalized eigenfunction of $\mathbf{K}$ corresponding to spectral parameter $\lambda = \exp(i\theta)$. Smoothed spectral measures $\{\xi(\theta) : \theta \in \Theta\}$.

ALGORITHM 2. Post-processing of Rigged DMD to compute generalized Koopman modes.[12]

Input: Snapshots $\mathbf{X}$, $\mathbf{Y}$, quadrature weights $\{w_m\}_{m=1}^{M}$, dictionary of observables $\{\psi_j\}_{j=1}^{N}$, $\{a_j\}_{j=1}^{m}$ with $\mathrm{Im}(a_j) > 0$, smoothing parameter $\varepsilon > 0$, angles $\Theta \subset [-\pi, \pi]_{\mathrm{per}}$, observables $\mathbf{g} = [g_1, \ldots, g_l]^T$.

1: Apply steps 1–5 of Rigged DMD (Algorithm 1) for each observable g_p to compute $\tilde{\mathbf{g}}_\theta^{(p)}$ (where the superscript denotes dependence on p) for $p = 1, \ldots, l$ and $\theta \in \Theta$.

2: For each $\theta \in \Theta$, compute the mean $\tilde{\mathbf{g}}_\theta = \frac{1}{l}\sum_{p=1}^{l}\tilde{\mathbf{g}}_\theta^{(p)}$ and the vector $\mathbf{c}_\theta \in \mathbb{C}^l$ defined component-wise by $[\mathbf{c}_\theta]_p = \tilde{\mathbf{g}}_\theta^*\tilde{\mathbf{g}}_\theta^{(p)}$.

Output: Vectors $\{\mathbf{c}_\theta : \theta \in \Theta\}$.

ALGORITHM 3. The kRigged DMD algorithm for computing spectral measures and generalized eigenfunctions of **K**.

Input: M_1 snapshots of 'training data' $\left\{\tilde{x}_m, \tilde{y}_m\right\}_{m=1}^{M_1}$, M_2 (distinct) snapshots of experimental data $\{\underline{x}_m, \underline{y}_m\}_{m=1}^{M_2}$, rank N, quadrature weights $\{w_m\}_{m=1}^{M_2}$, smoothing parameter $\varepsilon > 0$, polynomial order $n > 0$, observable g and a choice of kernel function $\mathscr{S}$. We will use angles $\theta \in \Theta$ for the spectral measure, while we use frequencies $f \in \mathscr{F}$ to approximate generalized eigenfunctions.

Stage A: Choose a kernel for the nonlinear dictionary and construct $\Psi_X^k \Psi_Y^k$

1: Use kEDMD with both datasets to generate a (potentially nonlinear) dictionary $\left\{\Psi_m^k\right\}_{m=1}^{N}$ where each $\Psi_m^k \in \mathbb{R}^{N,M_2}$.

Stage B: Build wave-packet approximations through sampling the resolvent.

1: Use this dictionary within the Rigged DMD algorithm (Algorithm 1) to generate a Koopman matrix $\mathbf{K}$, eigenvalues Λ, and eigenvectors $\mathbf{V}$.

2: Calculate observable coefficients $\mathbf{g} = (\mathbf{X}^{-1})^T \Psi_X^k \in \mathbb{R}^{d,N}$ and choose an observable vector $\underline{g} \in \mathbb{R}^N$ for the spectral measure.

3: For the spectral measure, follow stage B of Algorithm 1.

4: For generalized eigenfunctions evaluated at a frequency $f \in \mathscr{F}$, calculate the corresponding spectral angle via $\theta = 2\pi f \Delta t$, then use the post-processing method of Algorithm 2 for each angle θ to compute smoothed wave-packed approximations to modes $\mathbf{c}_\theta \in \mathbb{R}^d$.

Stage C: Calculate residuals associated with the spectral measure and/or the generalized eigenfunctions.

1: For each $\theta \in \Theta$, fix $\lambda = e^{i\theta}$ and find generalized eigenfunction $\mathbf{g}_\theta$ using Algorithm 1. Then calculate the relative residual $\mathrm{res}(\lambda, \mathbf{g}_\theta)$ from Eq. (18),

2: Repeat the previous step for every $\lambda = e^{2\pi f \Delta t i}$ where $f \in \mathscr{F}$ and the associated $\mathbf{g}_\theta$ eigenfunctions.

Output: A smoothed spectral measure $\left\{\xi(\theta) \,:\, \theta \in \Theta\right\}$ and smooth wave-packet approximations to generalized eigenfunctions $\left\{\mathbf{c}(f) \,:\, f \in \mathscr{F}\right\}$. Residuals for each approximate eigenfunctions and residuals for a subset $\Theta \in [-\pi, \pi]$

smoothing parameter $\varepsilon = 0.1$ in both cases and choose sixth-order polynomials.

We overlay the two spectral measures with the far-field noise PSD. We see good alignment for each of the two shedding frequencies. We chose eight frequencies to test by finding peaks existing or either or both spectra. These eight frequencies form our set $\mathscr{F}$, and we demonstrate their eigenfunctions for a Laplacian kernel dictionary of size $N = 3000$. We choose a large kernel to ensure that residuals are low for almost all frequencies. These residuals can be calculated by inserting $(\lambda, \mathbf{g}_\theta)$ pairs from Algorithm 3 into Eq. (18).

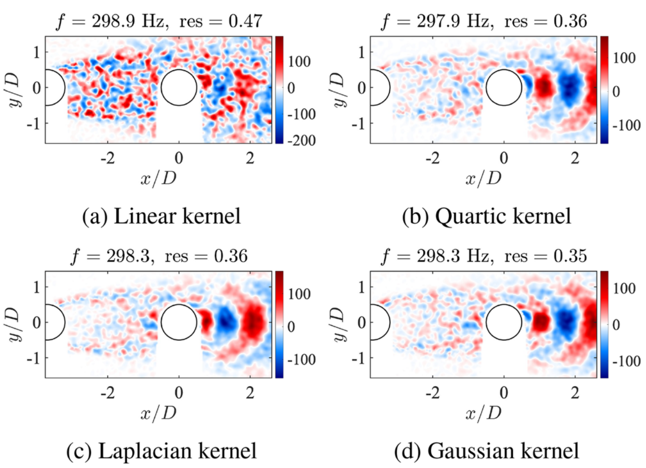

FIG. 22. High-rank modal comparison for the second harmonic to the first shedding frequency at ≈ 298 Hz.

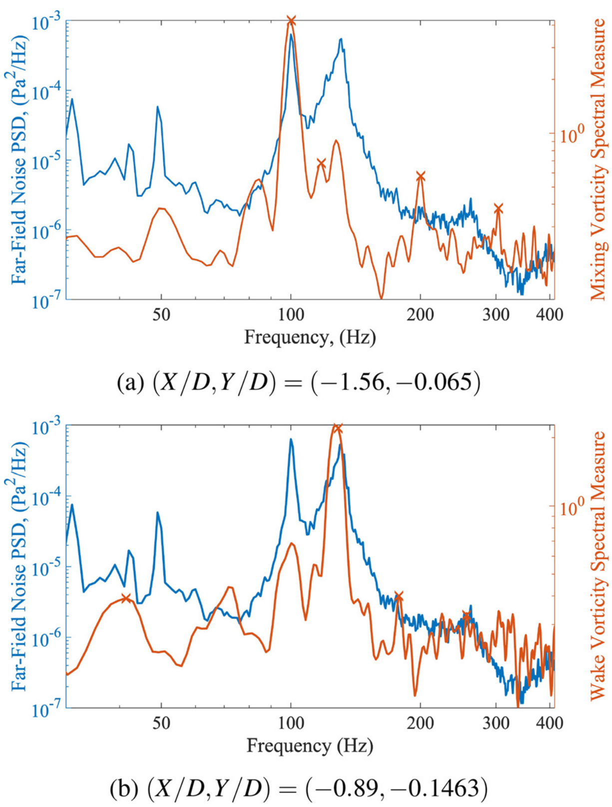

FIG. 23. Comparing the spectral measures of the vorticity signals located at a point between the cylinders (top) or in the wake of the second cylinder (bottom).

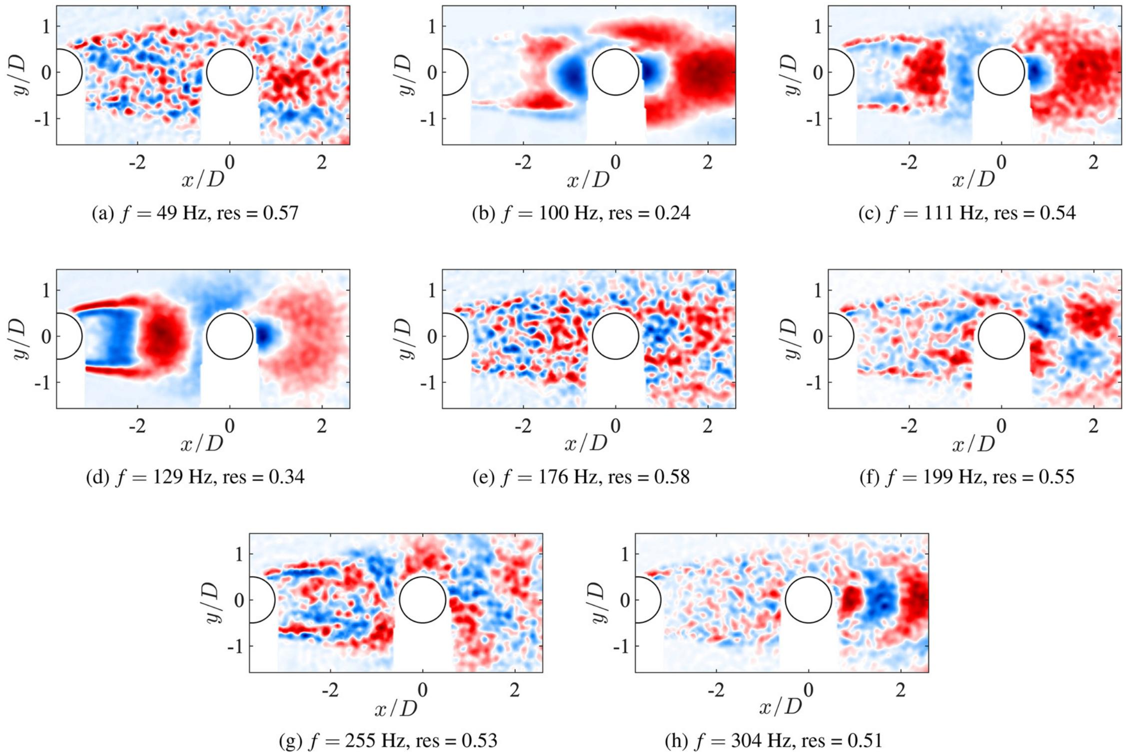

FIG. 24. kRiggedDMD eigenfunctions for several key frequencies using an $N = 3000$ Laplacian dictionary.

Figures 24(b), 24(d), and 24(f)–24(h) reproduce the key structures already discussed in previous sections. However, their direct relation to the spectral measure can give additional confidence when relating them to spectral peaks observed for the pressure data. The remaining figures [Figs. 24(a), 24(c), and 24(e)] represent less significant modes with weaker shedding strength. The benefit of Rigged DMD is that we do not have to rely explicitly on the output of a finite truncation of modes, and we can now control the smoothness of our general eigenfunction approximation. What is new to this paper is that these eigenfunctions are now a consequence of a better initial understanding of the system by using an improved dictionary that has been shown to capture the system behavior more clearly and accurately.

Finally, to justify our conclusions concerning the role of these structures, we plot the coherence $\gamma_{\omega,p_{ff}}$ between the vorticity field and far-field pressure signal in Fig. 25. This coherence is defined as

$$\gamma_{\omega,p_{ff}} = \frac{|S_{\omega,p_{ff}}(f)|^2}{S_{\omega,\omega}(f)\, S_{p_{ff},p_{ff}}(f)},$$

where $S_{\omega,p_{ff}}$ is the cross-spectral density between vorticity and far-field pressure, while $S_{\omega,\omega}, S_{p_{ff},p_{ff}}(f)$ are auto-spectral densities.

We restrict our attention to the two shedding and harmonic frequencies $f = 200$ and 297 Hz. We find the same patterns and large structures as seen in the modes from Figs. 8 and 9, suggesting this approach does have the potential for future studies.

VI. THE IMPACT OF NONLINEAR DICTIONARIES ON GENERALIZED EIGENFUNCTIONS

To finish, we turn our attention back to the importance of the dictionary chosen when using DMD methods. Specifically, we will compare and contrast the four kernels used within the Rigged DMD framework for the low- and mid-rank dictionary sizes. We compare eigenfunctions both qualitatively and quantitatively, using the subspace angle between eigenfunctions for the latter. The subspace angle is the

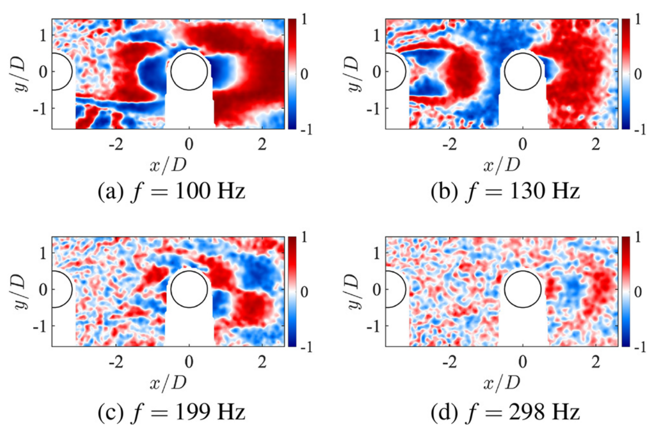

FIG. 25. Plots of the coherence $\gamma_{\omega,p_{ff}}$ between vorticity and far-field pressure.

angle between the subspaces defined by two vectors, such as the d-dimensional generalized eigenvectors. Angles close to zero suggest two modes are very similar, while angles closer to $\pi/2$ indicate that eigenvectors are increasingly distinct.

An alternative method for finding important modes is calculating the residuals for a representative subset $\Theta \in [-\pi, \pi]$ and sampling all residuals for corresponding points. In other words, one may calculate residuals for as much (or as little) of the unit circle as desired to find specific points of physical importance or with suitably low residuals.

To demonstrate this, we plot the frequency-residual lines for kRigged DMD with increasing rank N alongside the kEDMD modes with $N = 200$. Including kEDMD modes shows that we can now sample a continuum of values with no frequency restriction. For all kRigged DMD plots, we fix $\varepsilon = 0.15$ and choose polynomial order $n = 6$.

We gain plenty of insight from Fig. 26. First, we see the importance of a large dictionary size as an input to the kRigged DMD algorithm. However, a benefit to this is that for larger N, the average residual for the continuous approximation from kRigged DMD is *lower* than the average residual for kEDMD *for all four kernels*. This represents an improvement, thanks to the algorithm. We notice the advantage of nonlinear kernels in having larger residual troughs, meaning more frequencies near the key peaks can be sampled and give insight into transitions leading to or away from major phenomena. This is particularly clear at the harmonic frequencies for the first shedding frequency.

Using these plots, we will test and compare the predictions from the kernels at five frequencies. We pick frequencies close to (but not equal to) the significant modes where kEDMD may not have been able to provide nonspurious modes. We will test the results from a mid-rank approximation, $N = 1500$, and a high-rank approximation, $N = 3500$. The former has mostly high residuals but shows a larger difference between linear and nonlinear dictionaries. The latter has low residuals across the entire frequency range and can be considered much more reliable.

A. $N = 1500$ modes

To begin, we test a mid-rank approximation of $N = 1500$ modes.

Our first mode is for a low-frequency value of $f = 57$ Hz. Returning to Fig. 12, this mode would be expected to lie in between $\lambda = 1$ and the two low-residual shedding frequency modes. From the corresponding pseudospectra in Fig. 13, we know all kernels poorly capture this region. When comparing the predictions in Fig. 27, the best approximation appears to be from the quartic kernel. The most significant feature of the mode is the large structure shed downstream that has the most energy in Fig. 27(b). The subspace angles between the linear kernel and all nonlinear kernels are larger than 1.3, while the subspace angles between nonlinear kernels are between 1.14 and 1.18.

Figure 28 compares modes at frequency $f = 109$ Hz, for which the nonlinear kernels all have smaller residuals. These modes resemble Fig. 24(c) and show a similar transitional form between the first and second shedding modes from Figs. 24(b) and 24(d). The modes vary

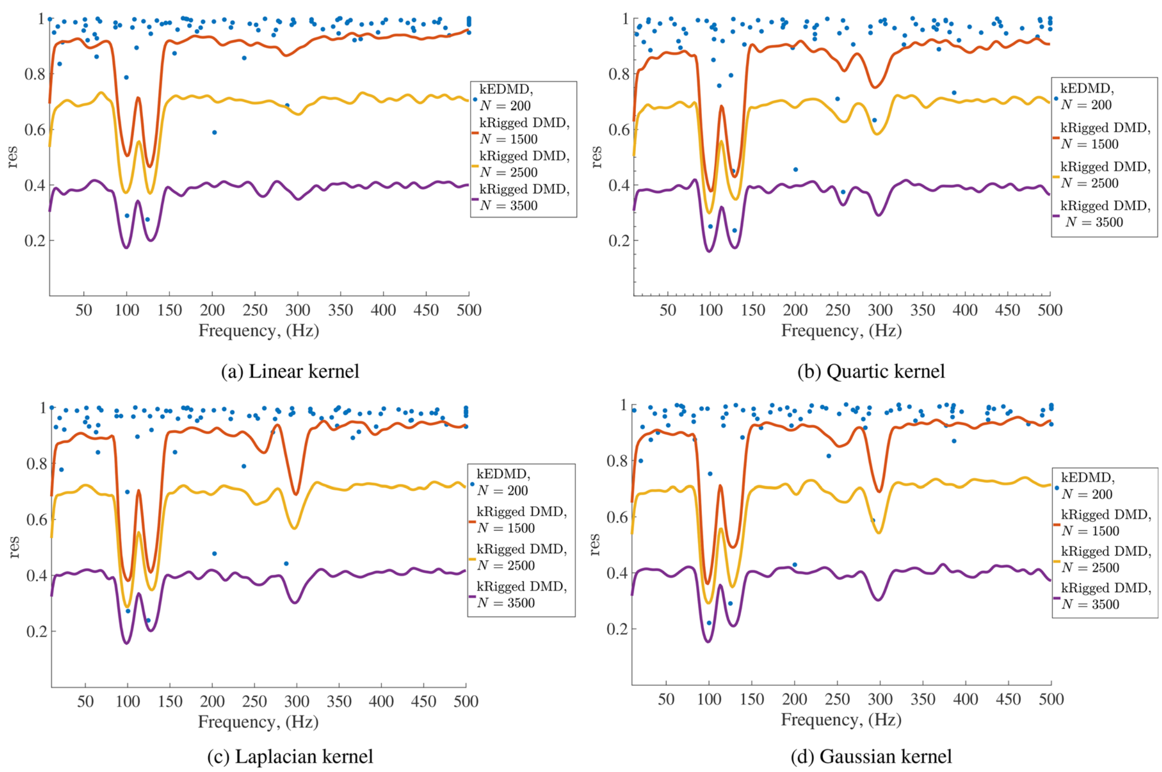

FIG. 26. Frequency-residual plot for four kernels with three dictionary sizes tested. Modes from the $N = 200$ kEDMD approximation with the same kernel are added for comparison.

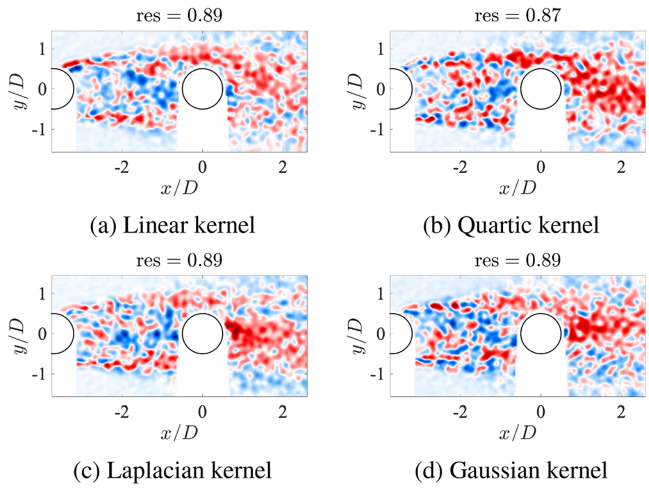

FIG. 27. kRigged DMD $N = 1500$ generalized eigenfunctions at $f = 57$ Hz.

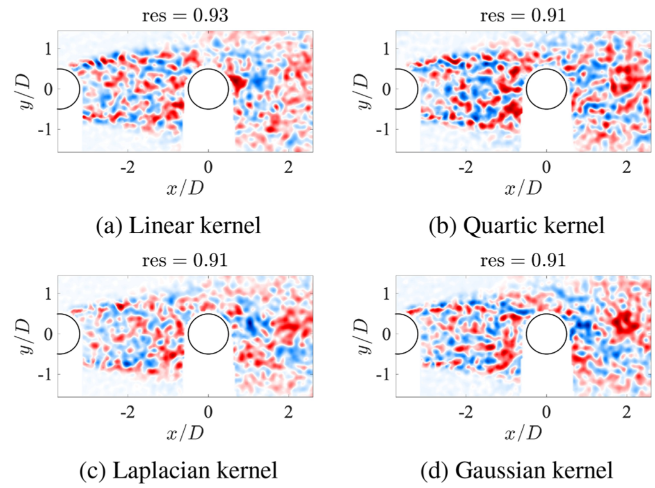

FIG. 29. kRigged DMD $N = 1500$ generalized eigenfunctions at $f = 190$ Hz.

primarily in the extent to which the upper and lower shear layers are attached. However, they generally show similar features and, therefore, have lower subspace angles. The largest subspace angle is 0.27 and is for the linear and quartic kernels, while the smallest is 0.21 and that is between the Laplacian and Gaussian kernels.

In Fig. 29, we approximate a generalized eigenfunction at $f = 190$ Hz. This is a value preceding the first harmonic for the first shedding frequency. All four kernels have poor residuals, with the Laplacian and Gaussian kernels giving slightly better results and recognizing the smaller structures shed from the downstream cylinder. This example shows significant variation between kernels. All subspace angles between linear and nonlinear kernels are greater than 1.42; however, the subspace angle between Laplacian and Gaussian kernels is 1.15.

For the fourth frequency, we choose $f = 261$ Hz, which has a large difference in residual between the linear and nonlinear kernels. This frequency is related to the first harmonic of the second shedding frequency, which is plotted in Figs. 21 and 24(g). When comparing Figs. 30(b) and 30(d) to Fig. 30(a), this may be attributed to the formation of structures in the gap alongside shear layers that break down as part of the bi-stability transition. For this example, most subspace angles are ≈ 1, excluding the angle between the Gaussian and Laplacian kernels, which is 0.89.

The final frequency to compare is *near* the third harmonic of the first shedding frequency, $f = 292$ Hz. Here, we see a significant benefit from nonlinear kernels. This time, the Gaussian kernel replicates the elongated structures shed by the downstream cylinder particularly well. It also shows less energy in the gap between the cylinders, as characterized by the reattachment regime. The larger residual in Fig. 31(a) may be due to incorrect predictions between the cylinders and the structures shed from the second cylinder having less distinct boundaries. This frequency shows larger disparity between linear and

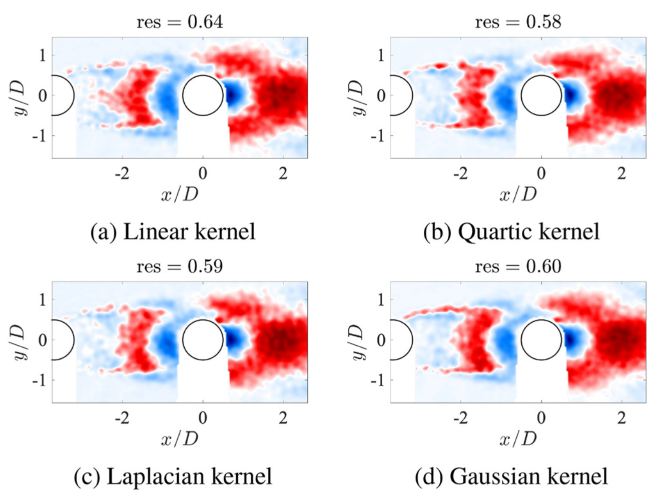

FIG. 28. kRigged DMD $N = 1500$ generalized eigenfunctions at $f = 109$ Hz.

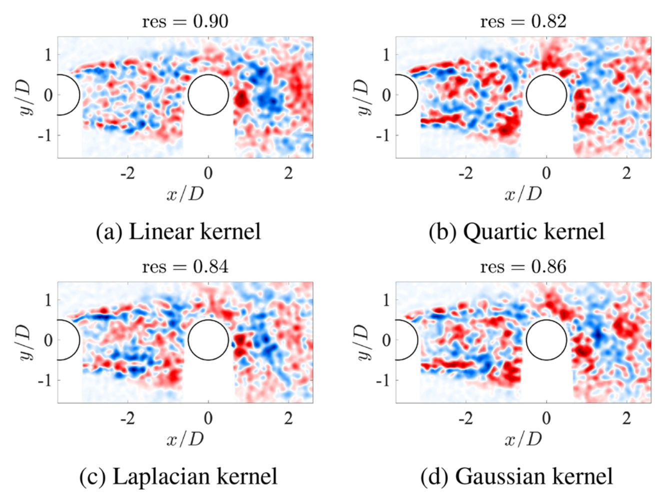

FIG. 30. kRigged DMD $N = 1500$ generalized eigenfunctions at $f = 261$ Hz.

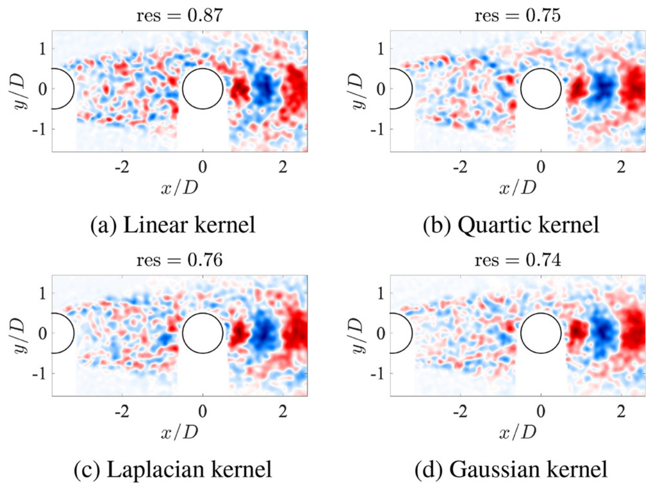

FIG. 31. kRigged DMD $N = 1500$ generalized eigenfunctions at $f = 292$ Hz.

nonlinear kernels, and this is reflected by subspace angles. All angles between linear and nonlinear kernels are greater than 0.77, while the angles between Gaussian and Laplacian are 0.54; the angle between Gaussian and quartic is 0.61, and the angle between Laplacian and quartic s 0.62.

B. $N = 3500$ modes

Now, we establish whether the differences between kernels remain for the $N = 3500$ high-rank dictionary size. From Fig. 26, all four kernels should approximate modes similarly well, but some disparities between the frequency-residual plots can be exploited. All kernels' underlying spectral measures are distinct since they capture features slightly differently. Hence, different levels of clarity are anticipated for less significant modes. This can be fine-tuned by choosing test frequencies based on the spectral measure instead of the pressure spectrum, but our approach is based on the converse.

With an increase in N, the residuals are halved for all kernels. The important feature is the structure occupying $x/D > 0$, which is now more similar for each kernel. The lower residual modes from Figs. 32(b) and 32(d) show a detachment of the upper shear layer downward toward the center of the cylinder. The qualitative similarity is supported by the subspace angle. The angle between linear and nonlinear kernels ranges between 1.04 and 1.08, much smaller than Fig. 27, while the smallest angle is 0.81, between the Laplacian and Gaussian kernel's eigenfunctions.

When comparing Figs. 28 and 33, the residuals are halved again. However, the initially low residuals from $N = 1500$ appear reliable compared to the high-rank modes. These modes support the hypothesis that the lower residual from the quartic kernel is due to its accurate approximation of the structure between the cylinders. The subspace angles are reduced, thanks to the increased accuracy due to the large N value. In fact, all subspace angles are between 0.13 and 0.16.

In Fig. 34, we can form more reliable observations on the flow modes preceding the first harmonic shown in Figs. 20 and 24(f). Although the region $x/D > 0$ appears similar, we notice a smaller and clearer structure that is positioned on the leeward side of the downstream cylinder around $y/D = -0.2$. This may indicate the final stages of breakdown in the co-shedding behaviors from the significant mode at $f = 130$ Hz. Thanks to kRigged DMD, closely inspecting such frequencies is now more reliably accessible. Regarding the subspace angles, they become much smaller than Fig. 29. Every pair decreases by approximately 0.35. The smallest angle this time is 0.96 and is between Gaussian and Laplacian eigenfunctions.

Figure 35 demonstrates the interplay between dictionary choice and frequencies. For a larger dictionary, we now see that for $f = 261$ Hz, the linear kernel is no longer the poorest choice for the generalized eigenfunction. It has the second-best residual. Naturally, it is possible to choose closely tailored frequencies within the vicinity of this value to optimize the residual for all kernels; however, this demonstrates the capabilities of both Rigged DMD and kRigged DMD for large N. The mode is consistent across all four kernels and varies only by the exact size and shape of the structure between shear layers that break down between the two cylinders. The consistent trend of

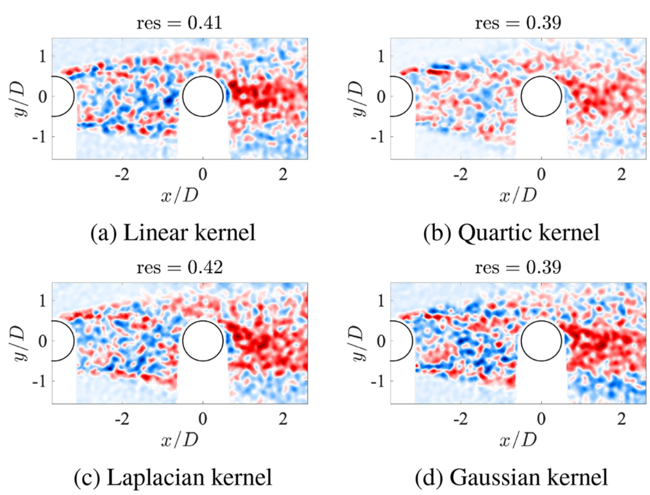

FIG. 32. kRigged DMD $N = 3500$ generalized eigenfunctions at $f = 57$ Hz.

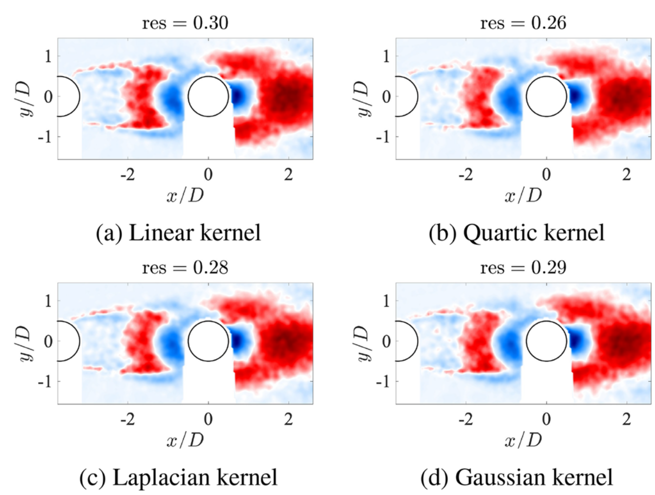

FIG. 33. kRigged DMD $N = 3500$ generalized eigenfunctions at $f = 109$ Hz.

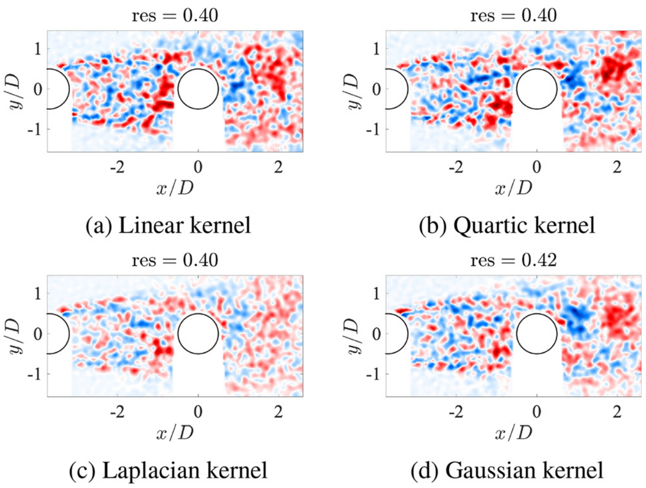

FIG. 34. kRigged DMD $N = 3500$ generalized eigenfunctions at $f = 190$ Hz.

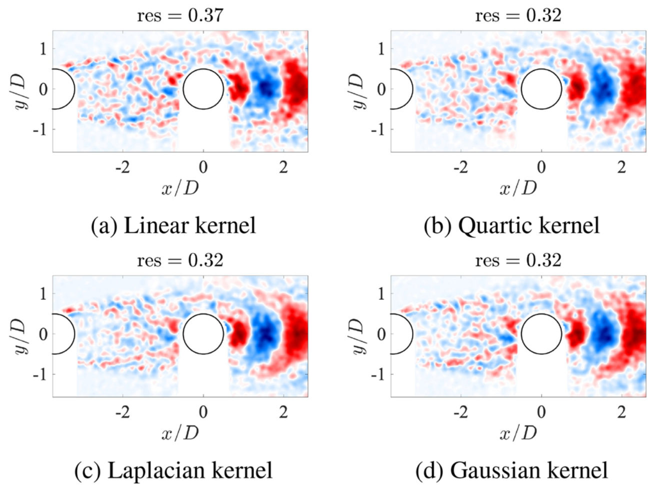

FIG. 36. kRigged DMD $N = 3500$ generalized eigenfunctions at $f = 292$ Hz.

subspace angles being largest between linear and nonlinear kernels is continued, and these angles are between 0.65 and 0.77. The smallest angle of 0.61 is between the Gaussian and Laplacian eigenfunctions.

Finally, Fig. 36 shows that the nonlinear kernels continue to capture the eigenfunction at $f = 292$ Hz better than the linear kernel. The significant difference between the linear and nonlinear kernels lies in correctly capturing the smaller structures lying in the gap between cylinders. The subspace angle between the linear and nonlinear eigenfunctions stays approximately 0.5, while the Gaussian and Laplacian eigenfunctions have a subspace angle of 0.36.

In summary, our exploration of the impact of N on generalized eigenfunctions from the kRigged algorithm primarily showed the trend that increasing N produces modes that are more and more accurate, and our comparisons of subspace angles support this. We found significant similarities between the Gaussian and Laplacian kernels, while the linear kernel has a higher residual and is more dissimilar to the nonlinear counterparts.

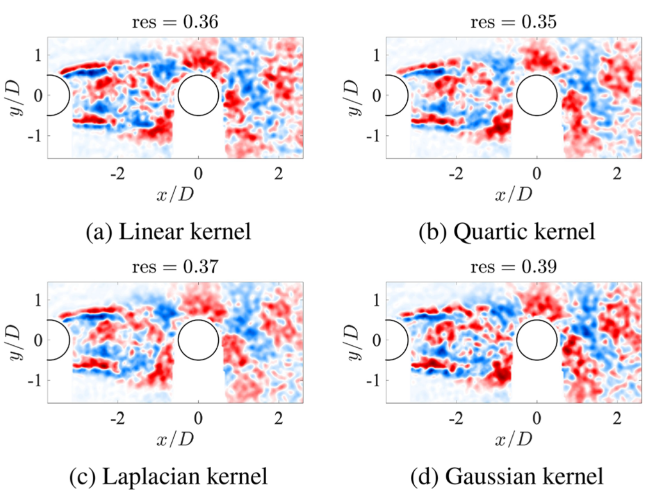

FIG. 35. kRigged DMD $N = 3500$ generalized eigenfunctions at $f = 261$ Hz.

VII. DISCUSSION

This study emphasizes the importance of a nonlinear dictionary, leading to developing a new DMD algorithm that can be used for numerous future applications in fluid mechanics and beyond. The experiment incorporated synchronized measurements of surface pressure, far-field noise, and velocity fields, providing a comprehensive dataset for modal decomposition analysis. We obtain two time-resolved velocity fields using PIV, from which the vorticity field was calculated and is used as the primary dataset for DMD. The experimental setup allowed us to explore the complex, nonlinear dynamics of the bi-stable flow and the connection between coherent structures in the velocity field and the far-field acoustics, contributing valuable insights to the field of aeroacoustics.

We used our experimental data to test the importance of nonlinear dictionaries within the kEDMD framework. Our findings demonstrate that using nonlinear dictionaries significantly enhances kEDMD's performance. These findings were influenced by computing and comparing the modal residual calculated using the ResDMD algorithm. These improvements influenced the creation of a novel algorithm, kRiggedDMD, in which a nonlinear dictionary is implemented within the traditional Rigged framework.

The importance of constructing larger, nonlinear dictionaries to be used within kRiggedDMD is evident when comparing individual modes. The successfully extracted modes were physically meaningful and instrumental in analyzing the complex vortical structures and flow dynamics characteristic of bi-stable configurations. Going forward, this efficiency and versatility will be a key advantage of the algorithm. Furthermore, for the first time, we applied residuals to the kRigged DMD framework. This provides a robust metric to assess and compare the quality of the extracted modes generated using different dictionaries. This new measure effectively evaluates how suitably the modes represent the underlying flow structures, adding error control to modes. This suggests that an effective strategy for choosing modes is to analyze frequency-residual plots that are freely sampled across the continuum of potential frequencies.

The strength of kRigged DMD lies in its flexibility. It allows for either the selection of user-defined modes or the rapid generation of spectral measures, and both can be used for further analysis. However, this approach relies heavily on the richness of the initial dictionary. Choosing a well-constructed dictionary is crucial for a successful modal decomposition. Future work could focus on further optimizing the dictionary selection. One may produce more dictionary comparisons using diverse datasets. Conversely, testing more tandem cylinder configurations involving cylinders of different sizes or shapes would also be interesting to see whether different kernels are more suited to representing specific phenomena. Such advancements would deepen the understanding of how nonlinear dictionaries influence mode extraction and could lead to improved modal decomposition techniques for multiple complex flow systems.

ACKNOWLEDGMENTS

A. D. G. Hales acknowledges support from EPSRC studentship EP/T517847/1 and the Virginia Tech Presidential Postdoctoral Fellowship.

AUTHOR DECLARATIONS

Conflict of Interest

The authors have no conflicts to disclose.

Author Contributions

A. D. G. Hales: Conceptualization (equal); Investigation (lead); Methodology (lead); Writing – original draft (lead); Writing – review & editing (equal). **M. J. Colbrook:** Conceptualization (equal); Project administration (lead); Supervision (lead); Writing – review & editing (equal). **C. Jiang:** Data curation (lead).

DATA AVAILABILITY

The data that support the findings of this study are available from the corresponding author upon reasonable request.

REFERENCES

[1]P. Schmid and J. Sesterhenn, "Dynamic mode decomposition of numerical and experimental data," Bull. Am. Phys. Soc. **53**, 1 (2008); available at https://meetings.aps.org/Meeting/DFD08/Event/91003.
[2]P. J. Schmid, "Dynamic mode decomposition of experimental data," in 8th International Symposium on Particle Image Velocimetry (PIV09), 2009.
[3]P. J. Schmid, "Dynamic mode decomposition of numerical and experimental data," J. Fluid Mech. **656**, 5 (2010).
[4]B. O. Koopman, "Hamiltonian systems and transformation in Hilbert space," Proc. Natl. Acad. Sci **17**, 315–318 (1931).
[5]B. O. Koopman and J. von Neumann, "Dynamical systems of continuous spectra," Proc. Natl. Acad. Sci. **18**, 255–263 (1932).
[6]C. W. Rowley, I. Mezić, S. Bagheri, P. Schlatter, and D. S. Henningson, "Spectral analysis of nonlinear flows," J. Fluid Mech. **641**, 115 (2009).
[7]M. J. Colbrook, "Numerical analysis meets machine learning," in *Handbook of Numerical Analysis* (Elsevier, 2024) Vol. 25, pp. 127–230.
[8]S. Bagheri, "Koopman-mode decomposition of the cylinder wake," J. Fluid Mech. **726**, 596 (2013).
[9]C. W. Rowley and S. T. M. Dawson, "Model reduction for flow analysis and control," Annu. Rev. Fluid Mech. **49**, 387 (2017).
[10]K. K. Chen, J. H. Tu, and C. W. Rowley, "Variants of dynamic mode decomposition: Boundary condition, Koopman, and Fourier analyses," J. Nonlinear Sci. **22**, 887 (2012).
[11]K. Taira, S. L. Brunton, S. T. M. Dawson, C. W. Rowley, T. Colonius, B. J. McKeon, O. T. Schmidt, S. Gordeyev, V. Theofilis, and L. S. Ukeiley, "Modal analysis of fluid flows: An overview," AIAA J. **55**, 4013 (2017).
[12]M. J. Colbrook, C. Drysdale, and A. Horning, arXiv:2405.00782 (2024).
[13]S. Singh, L. S. Ukeiley, L. N. Cattafesta, and K. Taira, "Extraction of DMD modes from pulse-burst PIV data of flow over an open cavity," AIAA Paper No. 2020-1068, 2020.
[14]A. Seena and H. J. Sung, "Dynamic mode decomposition of turbulent cavity flows for self-sustained oscillations," Int. J. Heat Fluid Flow **32**, 1098 (2011).
[15]H. Zhang, L. Zhou, T. Liu, Z. Guo, and F. Golnary, "Dynamic mode decomposition analysis of the two-dimensional flow past two transversely in-phase oscillating cylinders in a tandem arrangement," Phys. Fluids **34**, 033602 (2022).
[16]B. R. Noack, W. Stankiewicz, M. Morzyński, and P. J. Schmid, "Recursive dynamic mode decomposition of transient and post-transient wake flows," J. Fluid Mech. **809**, 843–872 (2016).
[17]Y. Yan, W. Chen, Z. Zhang, C. Ji, and N. Srinil, "Features and mechanisms of asymmetric wake evolution downstream of two parallel circular cylinders," Phys. Fluids **35**, 107132 (2023).
[18]M. M. Zdravkovich, "REVIEW—Review of flow interference between two circular cylinders in various arrangements," J. Fluids Eng. **99**, 618 (1977).
[19]D. Sumner, "Two circular cylinders in cross-flow: A review," J. Fluids Struct. **26**, 849 (2010).
[20]M. M. Zdravkovich, "The effects of interference between circular cylinders in cross flow," J. Fluids Struct. **1**, 239 (1987).
[21]T. Igarashi, "Characteristics of the flow around two circular cylinders arranged in tandem : 1st report," JSME Int. J. Ser. B **24**, 323 (1981).
[22]T. Igarashi, "Characteristics of the flow around two circular cylinders arranged in tandem : 2nd report, unique phenomenon at small spacing," JSME Int. J. Ser. B **27**, 2380 (1984).
[23]M. R. Khorrami, M. M. Choudhari, D. P. Lockard, L. N. Jenkins, and C. B. McGinley, "Unsteady flowfield around tandem cylinders as prototype component interaction in airframe noise," AIAA J. **45**, 1930 (2007).
[24]L. Jenkins, M. Khorrami, M. Choudhari, and C. McGinley, "Characterization of unsteady flow structures around tandem cylinders for component interaction studies in airframe noise," AIAA Paper No. 2005-2812, 2012.
[25]T. F. Geyer, E. Arcondoulis, and Y. Liu, "Experimental investigation of noise generation by porous coated tandem cylinder configurations," AIAA Paper No. 2021-2266, 2021.
[26]T. F. Geyer, "Experimental investigation of flow and noise control by porous coated tandem cylinder configurations," AIAA J. **60**, 4091 (2022).
[27]H. Liu, M. Azarpeyvand, J. Wei, and Z. Qu, "Tandem cylinder aerodynamic sound control using porous coating," J. Sound Vib. **334**, 190 (2015).
[28]E. Arcondoulis, T. F. Geyer, and Y. Liu, "An investigation of wake flows produced by asymmetrically structured porous coated cylinders," Phys. Fluids **33**(3), 037124 (2021).
[29]L. Ljungkrona, C. Norberg, and B. Sundén, "Free-stream turbulence and tube spacing effects on surface pressure fluctuations for two tubes in an in-line arrangement," J. Fluids Struct. **5**, 701 (1991).
[30]L. Ljungkrona and B. Sundén, "Flow visualization and surface pressure measurement on two tubes in an inline arrangement," Exp. Therm. Fluid Sci. **6**, 15–27 (1993).
[31]L. Wang, M. M. Alam, and Y. Zhou, "Two tandem cylinders of different diameters in cross-flow: Effect of an upstream cylinder on wake dynamics," J. Fluid Mech. **836**, 5-42 (2017); available at https://api.semanticscholar.org/CorpusID:126343693.
[32]N. W. M. Ko, P. T. Y. Wong, and R. C. K. Leung, "Interaction of flow structures within bistable flow behind two circular cylinders of different diameters," Exp. Therm. Fluid Sci. **12**, 33 (1996).
[33]R. Dubois and T. Andrianne, "Flow around tandem rough cylinders: Effects of spacing and flow regimes," J. Fluids Struct. **109**, 103465 (2022).
[34]R. Dubois and T. Andrianne, "Identification of distinct flow behaviours around twin rough cylinders at low wind incidence," J. Fluids Struct. **117**, 103815 (2023).
[35]G. Schewe and M. Jacobs, "Experiments on the flow around two tandem circular cylinders from sub-up to transcritical Reynolds numbers," J. Fluids Struct. **88**, 148 (2019).
[36]J. Lin, Y. Yang, and D. Rockwell, "Flow past two cylinders in tandem: Instantaneous and averaged flow structure," J. Fluids Struct. **16**, 1059 (2002).
[37]G. Xu and Y. Zhou, "Strouhal numbers in the wake of two inline cylinders," Exp. Fluids **37**, 248 (2004).
[38]M. M. Alam, Y. Zhou, and X. W. Wang, "The wake of two side-by-side square cylinders," J. Fluid Mech. **669**, 432–471 (2011).

[39]P. Burattini and A. Agrawal, "Wake interaction between two side-by-side square cylinders in channel flow," Comput. Fluids **77**, 134 (2013).
[40]C. H. S. Ehsan Adeeb and B. A. Haider, "Flow interference of two side-by-side square cylinders using IB-LBM – Effect of corner radius," Results Phys. **10**, 256 (2018).
[41]W. Y. Chang, G. Constantinescu, and W. F. Tsai, "Effect of array submergence on flow and coherent structures through and around a circular array of rigid vertical cylinders," Phys. Fluids **32**, 035110 (2020).
[42]Z. Khalifa, L. Pocher, and N. Tilton, "Regimes of flow through cylinder arrays subject to steady pressure gradients," Int. J. Heat Mass Transfer **159**, 120072 (2020).
[43]M. S. Ghazijahani and C. Cierpka, "Flow structure and dynamics behind cylinder arrays atReynolds number $\sim$100," Phys. Fluids **35**, 067125 (2023).
[44]C. Nicolai, S. Taddei, C. Manes, and B. Ganapathisubramani, "Wakes of wall-bounded turbulent flows past patches of circular cylinders," J. Fluid Mech. **892**, A37 (2020).
[45]T. E. Aasland, B. Pettersen, H. I. Andersson, and F. Jiang, "Revisiting the reattachment regime: A closer look at tandem cylinder flow at $Re = 10\,000$," J. Fluid Mech. **953**, A18 (2022).
[46]T. E. Aasland, B. Pettersen, H. I. Andersson, and F. Jiang, "Asymmetric cellular bi-stability in the gap between tandem cylinders," J. Fluid Mech. **966**, A39 (2023).
[47]C. Zeng, Y. Hu, J. Zhou, and L. Wang, "On the bi-stability of flow around two tandem circular cylinders at a subcritical Reynolds number of 3900," Phys. Fluids **36**, 105128 (2024).
[48]T. E. Aasland, B. Pettersen, H. I. Andersson, and F. Jiang, "Turbulent flow around convex curved tandem cylinders," J. Fluid Mech. **997**, A58 (2024).
[49]B. S. Carmo, J. R. Meneghini, and S. J. Sherwin, "Secondary instabilities in the flow around two circular cylinders in tandem," J. Fluid Mech. **644**, 395 (2010).
[50]Y. T. Wang, Z. M. Yan, and H. Wang, "Numerical simulation of low-Reynolds number flows past two tandem cylinders of different diameters," Water Sci. Eng. **6**, 433 (2013); available at https://api.semanticscholar.org/CorpusID:117188647.
[51]G. Palau-Salvador, T. Stoesser, and W. Rodi, "LES of the flow around two cylinders in tandem," J. Fluids Struct. **24**, 1304 (2008).
[52]G. V. Papaioannou, D. K.-P. Yue, M. S. Triantafyllou, and G. E. Karniadakis, "Three-dimensionality effects in flow around two tandem cylinders," J. Fluid Mech. **558**, 387 (2006).
[53]Q. Zhou, Md. Mahbub Alam, S. Cao, H. Liao, and M. Li, "Numerical study of wake and aerodynamic forces on two tandem circular cylinders at $Re = 10^3$," Phys. Fluids **31**, 045103 (2019).
[54]P. J. F. Clark and H. S. Ribner, "Direct correlation of fluctuating lift with radiated sound for an airfoil in turbulent flow," J. Acoust. Soc. Am. **46**, 802 (1969).
[55]T. E. Siddon, "Surface dipole strength by cross-correlation method," J. Acoust. Soc. Am. **53**, 619 (1973).
[56]H. K. Lee and H. S. Ribner, "Direct correlation of noise and flow of a jet," J. Acoust. Soc. Am. **52**, 1280 (1972).
[57]A. Henning, L. Koop, and K. Ehrenfried, "Simultaneous particle image velocimetry and microphone array measurements on a rod-airfoil configuration," AIAA J. **48**, 2263 (2010).
[58]A. Henning, K. Kaepernick, K. Ehrenfried, L. Koop, and A. Dillmann, "Investigation of aeroacoustic noise generation by simultaneous particle image velocimetry and microphone measurements," Exp. Fluids **45**, 1073 (2008).
[59]B. Lyu, "Canonical correlation decomposition of numerical and experimental data for observable diagnosis," AIAA Paper No. 2024-3206, 2024.
[60]P. J. Schmid, "Dynamic mode decomposition and its variants," Annu. Rev. Fluid Mech. **54**, 225 (2022).
[61]M. O. Williams, C. W. Rowley, and I. G. Kevrekidis, "A kernel-based method for data-driven Koopman spectral analysis," J. Comput. Dyn. **2**, 247 (2015).
[62]M. J. Colbrook, L. J. Ayton, and M. Szőke, "Residual dynamic mode decomposition: Robust and verified Koopmanism," J. Fluid Mech. **955**, A21 (2023).
[63]M. J. Colbrook, Q. Li, R. V. Raut, and A. Townsend, "Beyond expectations: Residual dynamic mode decomposition and variance for stochastic dynamical systems," Nonlinear Dyn. **112**, 2037 (2023).
[64]M. J. Colbrook, "Another look at residual dynamic mode decomposition in the regime of fewer snapshots than dictionary size," Physica D **469**, 134341 (2024).
[65]M. O. Williams, I. G. Kevrekidis, and C. W. Rowley, "A data–driven approximation of the Koopman operator: Extending dynamic mode decomposition," J. Nonlinear Sci. **25**, 1307 (2015).
[66]M. J. Colbrook and A. Townsend, "Rigorous data-driven computation of spectral properties of Koopman operators for dynamical systems," Commun. Pure Appl. Math. **77**, 221 (2023).
[67]D. Moreau, C. de Silva, R. Kisler, C. Tan, J. Jiang, M. Awasthi, and C. Doolan, in 23rd Australasian Fluid Mechanics Conference (23AFMC), 2022.
[68]M. Awasthi, "Sound radiated from turbulent flow over two and three-dimensional surface discontinuities," Ph.D. thesis (Virginia Tech, 2015).
[69]Y. Guan, C. R. Berntsen, M. J. Bilka, and S. C. Morris, "The measurement of unsteady surface pressure using a remote microphone probe," J. Visualised Exp. 53627 (2016).
[70]J. H. Tu, C. W. Rowley, D. M. Luchtenburg, S. L. Brunton, and J. Nathan Kutz, "On dynamic mode decomposition: Theory and applications," J. Comput. Dyn. **1**, 391 (2014).
[71]M. Lewin and É. Séré, "Spectral pollution and how to avoid it," Proc. London Math. Soc. **100**, 864 (2010).
[72]S. T. M. Dawson, M. S. Hemati, M. O. Williams, and C. W. Rowley, "Characterizing and correcting for the effect of sensor noise in the dynamic mode decomposition," Exp. Fluids **57**, 42 (2016).
[73]M. J. Colbrook, "The mpEDMD algorithm for data-driven computations of measure-preserving dynamical systems," SIAM J. Numer. Anal. **61**, 1585 (2023).